Geophysical Journal International

Geophys. J. Int. (2016) **206,** 1492–1514
Advance Access publication 2016 June 13
GJI Seismology

doi: 10.1093/gji/ggw206

The Showa Sanriku earthquake of 1933 March 2: a global seismological reassessment

Emile A. Okal,[1] Stephen H. Kirby[2] and Nikos Kalligeris[3]

[1]*Department of Earth and Planetary Sciences, Northwestern University, Evanston, IL* 60208, *USA. E-mail: emile@earth.northwestern.edu*
[2]*United States Geological Survey,* 345 *Middlefield Road, Menlo Park, CA* 94025, *USA*
[3]*Sonny Astani Department of Civil and Environmental Engineering, University of Southern California, Los Angeles, CA* 90089, *USA*

Accepted 2016 May 31. Received 2016 May 30; in original form 2016 March 5

SUMMARY

After 83 yr, the great normal-faulting earthquake of 1933 March 2, which took place off the Japan Trench and produced a devastating tsunami on the Sanriku coast and damaging waves in Hawaii, remains the largest recorded normal-faulting earthquake. This study uses advanced methods to investigate this event using far-field seismological and tsunami data and complements a sister study by Uchida *et al.* which used exclusively arrival times at Japanese stations. Our relocation of the main shock (39.22°N, 144.45°E, with a poorly constrained depth of less than 40 km) places it in the outer trench slope, below a seafloor depth of ∼6500 m, in a region of horst-and-graben structure, with fault scarps approximately parallel to the axis of the Japan Trench. Relocated aftershocks show a band of genuine shallow aftershocks parallel to the Japan Trench under the outer trench slope and a region of post-mainshock events landward of the trench axis that occur over roughly the same latitude range and are thought to be the result of stress transfer to the interplate thrust boundary following the normal-faulting rupture. Based on a combination of *P*-wave first motions and inversion of surface wave spectral amplitudes, we propose a normal-faulting focal mechanism ($\phi = 200°$, $\delta = 61°$ and $\lambda = 271°$) and a seismic moment $M_0 = (7 \pm 1) \times 10^{28}$ dyn cm ($M_w = 8.5$). A wide variety of data, including the distribution of isoseismals, the large magnitudes (up to 8.9) proposed by early investigators before the standardization of magnitude scales, estimates of energy-to-moment ratios and the tentative identification of a *T* wave at Pasadena (and possibly Riverside), clearly indicate that this seismic source was exceptionally rich in high-frequency wave energy, suggesting a large apparent stress and a sharp rise time, and consistent with the behaviour of many smaller shallow normal-faulting earthquakes. Hydrodynamic simulations based on a range of possible sources consistent with the above findings, including a compound rupture on two opposite-facing normal-faulting segments, are in satisfactory agreement with tsunami observations in Hawaii, where run-up reached 3 m, causing significant damage. This study emphasizes the need to include off-trench normal-faulting earthquake sources in global assessments of tsunami hazards emanating from the subduction of old and cold plates, whose total length of trenches exceed 20 000 km, even though only a handful of great such events are known with confidence in the instrumental record.

Key words: Tsunamis; Earthquake source observations; Intra-plate processes.

PROLOGUE

In the early morning of Thursday 1933 March 2, shortly after 07:00 Hawaiian Standard Time,[1] Austin E. Jones, a Staff Seismologist, was on station at the Hawaiian Volcano Observatory, on the rim of Kilauea, where a Bosch-Omori seismograph had been originally deployed in 1913. Meanwhile, Captain Robert V. Woods, a retired shipmaster, was in charge of another seismic station of the Hawaiian Volcano Research Association in the basement of his house in Kealakekua on the Kona Coast (Jaggar 1933). Both operators noted that a great distant earthquake was being recorded by their instruments (Fig. 1). In a telephone conversation that morning, and based on $S - P$ time intervals, the two observers estimated that the

[1] In 1933, Hawaiian Standard Time (HST) was GMT −10:30.

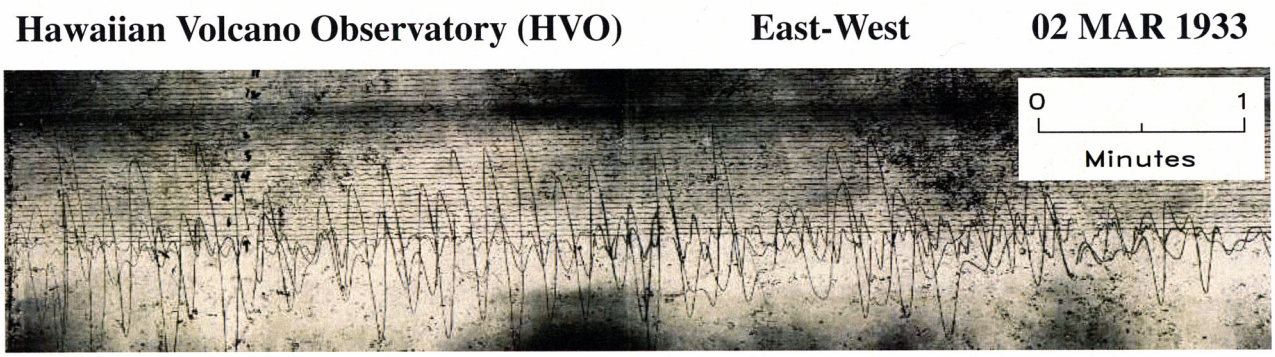

Figure 1. Hawaiian Volcano Observatory seismogram of the Showa Sanriku earthquake. This is a 368-s excerpt of the east–west component of the Bosch-Omori seismogram. Time runs left and down; there are four traces to the hour. The interpretation of this record as signaling a 'big and far' event led HVO Staff to issue a tsunami warning, followed by a successful evacuation.

earthquake had originated off the coast of Japan, and that it could generate a tsunami that would arrive around 15:30 HST. By 10:00 HST, they had notified the coastal authorities in Hilo and Kailua. Around noon, radio reports confirmed the occurrence of a devastating nighttime earthquake and tsunami on the Sanriku coast of Japan, whose final death toll would be horrific (3066 dead and missing).

A successful evacuation took place on the 'Big' Island of Hawaii, with cargo moved inland from docks, and many boats pulled onshore or sent out to sea. Tsunami waves reached the Kona coast at 15:20 HST and Hilo harbor at 15:36, running up to as high as 3.2 m; they started with a leading depression, and lasted for many hours. Despite some structural damage notably on the Kona coast, destruction was minimized and no lives were lost in Hawaii, thanks to the timeliness of the scientists' alert, and to the proactive response of the population involved. The latter might have been helped by the memory of the 1923 Kamchatka tsunami, for which a warning issued by T.A. Jaggar under a comparable timeline had been ignored by local authorities (Jaggar 1930), causing significant damage and one death in Hawaii.

We choose to highlight this episode because it constitutes the first example of a successful tsunami warning and evacuation in the far field, based on the analysis of seismic waves. It is remarkable that this warning (and to some extent the unheeded one in 1923) was carried out on what would constitute, by today's standards, a scientific and technological shoestring. It took place before the development of the concepts of plate tectonics and subduction zones, even before the introduction of the concept of seismic magnitude (Richter 1935), and of course long before real-time worldwide communications brought us instant coverage of far-flung disasters, as in the case of the 2011 Tohoku catastrophe. The 1933 evacuation was triggered by no more than the staff seismologists' visionary interpretation of a 'far and big' event, a basic knowledge of propagation velocities for seismic and tsunami waves and the availability of a few telephone lines throughout the island.

Even more remarkable is the fact, pointed out by Kanamori (1971), that the 1933 Sanriku earthquake was not a so-called interplate mega-thrust event expressing relative motion between colliding tectonic plates, but rather a normal-faulting event resulting from rupture inside the oceanic lithosphere. In this respect, the occurrence of such an event in modern times would transcend any of the increasingly popular probabilistic estimates of far-field tsunami risk based on recurrence rates of interplate events. It is paramount to keep in mind that this class of intra-plate events, although still poorly understood especially regarding their slow recurrence rates, can and will export death and destruction across oceanic basins, and must therefore be taken into account in the estimation of global tsunami hazards. It is in this context that we present here a modern seismological reassessment of the 1933 Showa Sanriku earthquake.

1 INTRODUCTION

With a published moment of 4.3×10^{28} dyn cm (Kanamori 1971), the 'Showa Sanriku' earthquake of 1933 March 2 is the largest event known to occur in an 'outer trench slope' normal-faulting geometry, that is, in an intraplate context, seawards of the trench delineating the subduction system. Such events are actually quite rare, with only three entries of moment greater than 10^{28} dyn cm in the Global CMT catalogue: the earthquakes of 1977 August 19 in Sumba, 2007 January 13 in the Kuril Islands and 2009 September 29 South of Samoa. Among those, the Samoa event was a composite one, featuring a normal-faulting initiator followed by an interplate subevent that occurred along the bend of the Tonga-Samoa subduction zone (Li *et al.* 2009; Lay *et al.* 2010). The Kuril event took place by stress transfer, following by two months a larger interplate thrust earthquake (Ammon *et al.* 2008), of which it cannot be regarded as a 'genuine' aftershock, since it occurred neither on the same fault nor with the same mechanism as the main shock.

Prior to the digital era, a few more examples of large outer rise earthquakes are known, such as the South Sandwich event of 1929 June 27, and in the Aleutian, the Fox Islands earthquake of 1929 March 7 and the Rat Island one of 1965 March 30. The former occurred in the 'STEP' geometry (Govers & Wortel 2005), along a lateral tear of the South American plate at the northern margin of the South Sandwich arc, while the Rat Island one took place as a non-'genuine' aftershock of the great earthquake of 1965 February 4 (Stauder 1968a,b). The Fox Islands event may have occurred farther out at sea, below the outer rise. Definitive focal mechanisms and moments have been published for both the South Sandwich and Rat Island events (Abe 1972; Okal & Hartnady 2009). Table 1 regroups source data for the seven earthquakes discussed above.

Another important aspect of normal-faulting earthquakes in the neighbourhood of oceanic trenches is that even though their focal mechanisms do not directly represent the process of subduction, that is, the sinking of one lithospheric plate below another one, they nevertheless express the flexure associated with the downward deflection of the plate as a result of its subduction into the oceanic trench and under the overlying plate. The interpretation of this ancillary deformation confirmed the concept of subduction as a universal process in the global model of plate tectonics (Stauder 1968a,b).

Table 1. Major outer rise normal-faulting earthquakes.

Date D M (J) Y	Region	Epicentre (°N)	(°E)	Source†	Moment (10^{28} dyn cm)	Focal mechanism ϕ, δ, λ (°)	Context	Reference
07 March (066) 1929	Fox Islands	51.35	−177.91	a	0.7	244, 59, −120*		Kanamori (1972)
27 June (178) 1929	South Sandwich	−54.53	−29.54	b	1.7	71, 70, −88	STEP	Okal & Hartnady (2009)
02 March (061) 1933	Sanriku	39.22	144.45	c	7.0	200, 61, −89		This study
30 March (089) 1965	Aleutian	50.32	177.93	a	0.34	104, 47, −118	Post-shock	Abe (1972)
19 August (231) 1977	Sumba	−11.18	118.37	a	3.6	260, 24, −73		Dziewoński *et al.* (1987)
13 January (013) 2007	Kuril	46.17	154.80	d	1.8	43, 59, −115	Post-shock	Global CMT
29 September (272) 2009	Samoa	−15.13	−171.97	d	1.7	346, 62, −63	Composite	Li *et al.* (2009)

†Sources for epicentral data:
a: Engdahl & Villaseñor (2002).
b: Okal & Hartnady (2009).
c: This study.
d: Global CMT project.
*By analogy (Kanamori 1972) with the nearby and comparable event of 1965 July 29 (Stauder 1968a).

However, large normal-faulting off-trench earthquakes remain rare: Table 1 lists only five such events with $M_0 > 10^{28}$ dyn cm during the instrumental era. There have probably been more, that have been mistaken for interplate thrust or intraslab shocks before global epicentres were accurate enough to definitively place them oceanward of trenches. During the same period of observation, there have been about 20 times that number of great interplate thrust subduction earthquakes (i.e. about one every year). Furthermore, we note that outer trench slope earthquakes of that size are unknown where the age of the incoming oceanic lithospheric plate is Tertiary or younger, such as in the Eastern Pacific (Cascadia, Central and South America).

This striking contrast between the occurrence of both types of events is not unexpected, and can be explained on several accounts. First, normal faults are estimated to slip at rates slower than 1 mm yr^{-1}, based on scarp evolution (Kirby *et al.*, in preparation). In addition, for young subducting plates, the maximum depths of associated normal-faulting ruptures are very shallow, which essentially hampers the development of a large rupture necessary to host a great earthquake. Also, for a given convergence rate, the younger and thinner the plate, the lower the maximum bending strain and strain rate will be (Kirby *et al.*, in preparation). Finally, this age restriction on large flexural earthquakes clearly does not apply to great interplate thrust events, many of which occur at subduction zones featuring young oceanic lithosphere (e.g. Chile 1960).

In this general context, the purpose of this paper is to conduct a series of modern reassessments of the 1933 Sanriku earthquake. By relocating the main event and its aftershocks, we seek to document the size of its rupture, and to interpret it in the local tectonic context; by obtaining a moment tensor solution at mantle periods, we constrain the true size of the event and the mechanism of generation of its tsunami. Through a better understanding of the 1933 event, we also aim to gain further insight into the tsunami hazard posed by this class of shocks, of which the Showa Sanriku earthquake was the largest recorded.

2 RELOCATIONS

2.1 The main shock, 1933 March 2, 17:30 GMT

We relocated the main shock using travel times listed in the International Seismological Summary (ISS) and the interactive iterative method of Wysession *et al.* (1991); the latter includes a Monte Carlo algorithm which injects Gaussian noise into the data set of arrival times, in order to define a confidence ellipse. For events in the early 1930s, we give this noise a standard deviation $\sigma_G = 5$ s. The event relocates to 39.22°N, 144.45°E, with a Monte Carlo ellipse of semi-major axis 20 km, oriented NW-SE. The solution retains 200 arrival times (out of 206 originally considered), with a root-mean-squares residual $\sigma = 3.1$ s. This solution, plotted as the star on Fig. 2, is obtained with a constrained depth of 10 km. All attempts to let the depth float led to a surficial source. Following Rees & Okal (1987), we also examined the variance reduction of constrained-depth relocations as a function of source depth. Fig. 3 shows a regular trend of residuals increasing with depth, especially beyond 40 km. However, this trend remains weak, and we conclude that the available data set lacks depth resolution in the upper 40 km of the plate. The small dots extending west of the star on Fig. 2(b) express the small move-out of the epicentre when the constrained depth is increased from 10 to 40 km. Note that the epicentres inverted at those trial depths remain inside our original Monte Carlo ellipse, and that seafloor depths at the relevant epicenters range from 6500 to 7000 m.

Fig. 2(b) compares our results with previous epicentral estimates. Of particular interest is Matuzawa's (1935) location at 39.15°N, 144.40°E, which falls inside our Monte Carlo ellipse; a modern relocation of his published phase data, using Wysession *et al.*'s (1991) algorithm, converges on 39.33°N, 144.38°E (194 stations, $\sigma = 3.7$ s), only 20 km north of his original epicentre, which underscores the amazing precision of historical relocations carried out with pencil and paper in the 1930s. Gutenberg & Richter's (1954) solution (which they rounded to the nearest quarter degree at 39.25°N, 144.5°E) also locates inside our error ellipse, as does Kanamori's (1971) estimate (39.27°N; 144.51°E) obtained from a computerized inversion. The ellipse also grazes Engdahl & Villaseñor's (2002) epicentre at 39.22°N, 144.62°E, the latter using a constrained depth of 35 km. All the above solutions used data sets that included teleseismic arrivals.

By contrast, locations obtained from exclusively regional data sets, such as Honda & Takehana's (1933) estimate (39.23°N, 144.87°E; 'HT', diamond on Fig. 2) or the 1957 JMA solution (39.13°N, 145.12°E; open square on Fig. 2) are offset systematically to the east, the latter more than 50 km, to a location below the outer rise, in a geometry which would be comparable to that of the 1929 Fox Islands Event. The origin of this systematic bias is discussed in a companion paper (Uchida *et al.* 2016).

In summary, our preferred epicentre for the 1933 main shock, together with most other published solutions, is clearly located on the outer slope of the trench, at a seafloor depth of ∼6500 m, in a

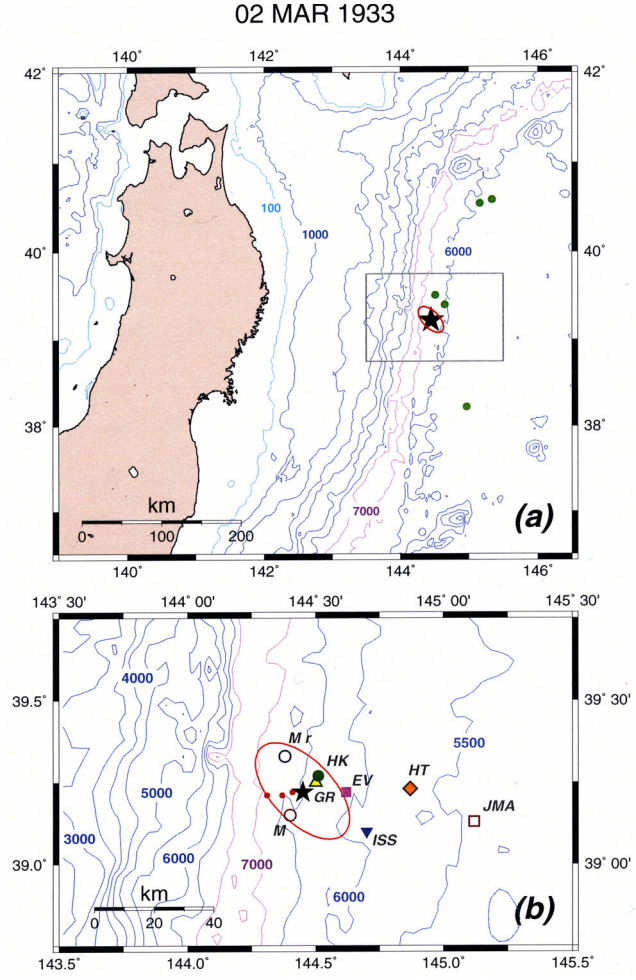

Figure 2. Relocation of the 1933 main shock. (a) General situation map. Isobaths are at 100 m, 1000 m and then every 1000 m. The green dots are normal-faulting epicenters from the GlobalCMT catalogue (1976–2011), and occurring eastwards of the trench. The grey box outlines the bottom frame. (b) Close-up of epicentral area in the vicinity of the Sanriku Trough. Isobaths are at 500 m intervals. Our relocation is shown as the black star, with associated Monte Carlo ellipse. Other locations are from the ISS (inverted triangle), Honda & Takehana's (1933) (*HT,* diamond), Matuzawa (1935) (*M*, red open circle, with our relocation of his data set (*M r*) shown as the black open circle), Gutenberg & Richter (1954) (*GR*, triangle), Kanamori (1971) (*HK*, solid circle) and Engdahl & Villaseñor (2002) (*EV,* solid square). The JMA location (open square) is about 40 km to the east. The small dots extending west from our relocation express the moveout of the epicentre when the constrained depth is increased from 10 to 40 km by increments of 10 km.

geometry reminiscent of the 1965, 1977 and 2007 events listed in Table 1.

2.2 Aftershocks

The 1933 earthquake was followed by a large number of aftershocks, which can be interpreted as continuing to this day, as exemplified, in the GlobalCMT database, by five normal-faulting solutions ($M_0 \geq 10^{24}$ dyn cm; green dots on Fig. 2a), occurring east of the Trench and between 1978 and the great Tohoku earthquake in 2011. In this study, we limit ourselves to the 93 events listed by the ISS for the year 1933 in the area delimited on Fig. 2, including six foreshocks.

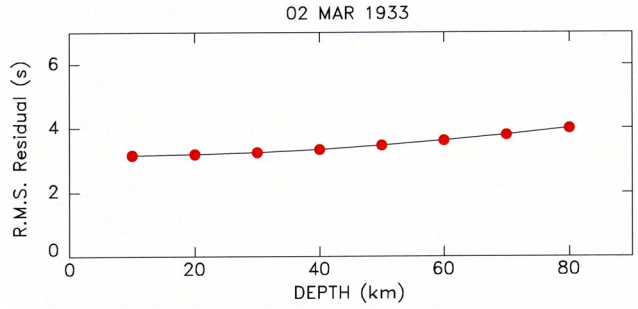

Figure 3. Root-mean-squares residual as a function of depth for constrained-depth relocations of the 1933 main shock. Note the weak increase of rms with depth, especially for the shallowest solutions.

Most relocations were carried out at a constrained depth of 10 km. While in a number of favourable cases, floating depth relocations could converge (and their results are listed in Table 2), the resulting depths were not robust during Monte Carlo tests run with unconstrained depths, whose solutions extended from the surface to as far deep as 200 km, and thus the data set in Table 2 should be viewed as having essentially no depth control.

The full data set of relocated epicentres is presented on Fig. 4(a), while Fig. 4(b) regroups only those 22 events located with a minimum of 30 stations, shown with their associated Monte Carlo ellipses. It is immediately apparent that among these well-located events, only five (A54, A66, A73, A74 and possibly A84) can legitimately be considered as genuine aftershocks occurring seaward of the trench, and thus within the area of rupture of the main shock. They would suggest a figure of 170 km for the length of faulting *L* along the outer rise of the trench. The Monte Carlo ellipses of all 17 remaining well-located events are fully contained west of the subduction system, and thus these earthquakes must be considered as non-genuine aftershocks, triggered on different fault systems by a mechanism of stress transfer (Stein 1999; Lin & Stein 2004). Similarly, the six foreshocks relocated as part of this study took place on the landward side of the trench on what must have been different fault systems. Note that the largest aftershock (1933 June 18; A70 in Table 2) occurred landward of the accretionary prism, only 50 km from the Japanese coastline. As discussed in Section 4, it could express thrust faulting along the slab interface, possibly triggered by stress transfer from the main shock.

The pattern featured by this distribution is in general agreement with the results of Uchida *et al.* (2016), who relocated a larger number of events (183) based exclusively on regional (Japanese) arrivals, and using a customized 3-D velocity structure. Both studies point to a bimodal distribution of aftershocks, featuring a ∼170-km-long cluster on the seaward side of the trench which we regard as genuine aftershocks, and a separate group of events landward of the trench, some (but not all) of which may be associated with interplate motion. It is interesting to note that, out of 61 common events, 29 of Uchida *et al.*'s (2016) epicentres fall within our relevant Monte Carlo ellipse, and in nine more instances, their confidence ellipse intersects ours. Out of the remaining 23 aftershocks, 11 have the two ellipses approaching each other within 20 km and 11 more are smaller events located with fewer than 15 arrival times. In conclusion, and even though the two studies involved different phase data sets, methodologies and crustal models, their results are generally compatible.

Finally, we note that only three aftershocks (Events A48, A70 and A74) were relocated by Engdahl & Villaseñor (2002) as part of their Centennial catalogue. These are shown in blue on Fig. 4(b), with

Table 2. Results of relocations performed in this study.

Number *	Date D M (J) Y	Origin time GMT	Epicentre (°N)	(°E)	Depth (km)	Code†	Stations Read	Used	rms (s)	Focal mechanism††	Magnitude M_{PAS}
F01	03 January (003) 1933	15:27:05.7	40.81	143.50	10	C	59	53	3.5		$6\frac{1}{4}$
F02	07 January (007) 1933	4:06:42.6	40.55	143.32	10	C	116	113	4.6		$6\frac{1}{2}$
F03	07 January (007) 1933	4:53:44.1	40.33	143.86	10	C	25	23	2.6		
F04	07 January (007) 1933	20:07:50.9	40.41	143.50	10	C	23	20	2.8		
F05	20 February (051) 1933	9:51:09.1	37.01	142.54	20	F	59	49	3.7		
F06	20 February (051) 1933	14:17:38.0	36.82	142.30	20	C	7	7	3.3		
M07	**02 March (061) 1933**	**17:30:57.3**	**39.22**	**144.45**	**10**	**C**	**206**	**200**	**3.1**	**N**	**8.9**
A08	02 March (061) 1933	18:26:18.2	39.56	143.67	10	C	20	14	3.8		
A09	02 March (061) 1933	19:41:38.2	39.79	144.27	10	C	14	14	5.4		
A10	02 March (061) 1933	20:42:55.8	39.46	143.26	10	C	33	30	4.2	a	$6\frac{1}{2}$
A11	02 March (061) 1933	21:48:21.8	39.55	143.38	30	C	7	7	5.3	a	
A12	02 March (061) 1933	22:34:51.3	40.51	143.31	30	C	11	11	3.4	a	
A13	03 March (062) 1933	0:18:18.9	40.04	143.11	10	C	12	9	3.3		
A14	03 March (062) 1933	4:37:46.1	38.95	144.10	10	C	25	23	3.1	a	
A15	03 March (062) 1933	9:12:51.7	39.24	143.27	10	C	53	53	3.3	a	$6\frac{1}{2}$
A16	03 March (062) 1933	9:38:40.8	39.64	143.44	10	C	23	22	2.0		
A17	03 March (062) 1933	10:32:17.0	39.59	143.39	10	C	17	16	2.9	a	
A18	03 March (062) 1933	11:46:40.5	35.64	140.79	68	F	8	8	2.2		
A19	03 March (062) 1933	11:56:36.1	39.59	143.23	2	F	17	16	4.7	a	
A20	03 March (062) 1933	12:13:48.4	38.65	144.56	13	F	18	18	2.4	a	
A21	03 March (062) 1933	15:02:21.2	39.75	143.33	80	F	23	20	3.8	a	
A22	03 March (062) 1933	15:07:14.6	39.61	143.17	10	C	19	13	3.3		6
A23	03 March (062) 1933	15:50:57.7	38.68	142.24	10	C	10	7	5.2	a	
A24	03 March (062) 1933	16:11:47.3	39.30	144.65	62	F	15	14	1.3	a	
A25	03 March (062) 1933	18:47:31.8	40.63	142.01	10	C	7	6	5.9	a	
A26	03 March (062) 1933	19:07:24.6	39.92	143.70	12	F	15	13	5.0	a	
A27	03 March (062) 1933	19:50:43.7	39.56	142.61	71	F	8	8	2.7	a	
A28	03 March (062) 1933	20:20:24.1	39.61	143.15	10	C	6	6	1.8	a	
A29	04 March (063) 1933	6:44:37.2	40.67	141.85	68	C	7	6	3.8	a	
A30	04 March (063) 1933	6:44:53.6	40.14	143.89	10	C	5	5	2.8		
A31	04 March (063) 1933	12:40:08.7	39.00	144.70	49	F	9	8	1.9	k	
A32	04 March (063) 1933	20:27:37.4	39.07	144.78	42	F	8	8	3.0	a	
A33	07 March (066) 1933	22:21:27.8	39.63	144.52	35	C	11	10	2.9	a	
A34	08 March (067) 1933	1:35:41.5	39.82	143.40	10	C	28	27	3.6	k	
A35	12 March (071) 1933	5:05:51.6	40.16	143.86	10	C	12	11	5.0	a	6
A36	13 March (072) 1933	7:15:00.1	35.92	142.32	10	C	14	12	4.5		
A37	13 March (072) 1933	15:57:01.1	39.39	144.60	10	C	7	6	5.4		
A38	14 March (073) 1933	12:58:58.8	37.93	144.45	10	C	9	8	4.6		
A39	14 March (073) 1933	16:04:46.2	40.00	144.24	10	C	9	7	5.4		
A40	21 March (080) 1933	15:54:00.6	38.49	141.75	66	F	24	23	1.4	k	
A41	21 March (080) 1933	17:11:04.2	36.53	141.77	10	C	6	6	1.4		
A42	23 March (082) 1933	12:42:50.6	39.57	144.64	10	C	12	10	4.9	a	
A43	01 April (091) 1933	15:58:59.7	39.67	143.28	10	C	69	69	3.0	a	6
A44	01 April (091) 1933	22:40:53.1	39.28	145.01	10	C	24	22	3.9	k	
A45	02 April (092) 1933	9:52:44.5	36.47	140.71	39	F	33	32	2.5		
A46	02 April (092) 1933	10:10:39.9	40.11	142.92	71	F	10	9	3.0	a	
A47	06 April (096) 1933	15:11:56.7	39.43	144.18	62	F	9	8	3.2	a	
A48	09 April (099) 1933	2:46:37.0	39.33	143.54	10	C	43	42	3.5	a	$6\frac{3}{4}$
A49	09 April (099) 1933	2:57:17.0	39.39	143.74	10	C	6	5	3.2	a	
A50	09 April (099) 1933	6:27:49.4	39.86	144.02	10	C	4	4	2.1	a	
A51	09 April (099) 1933	10:30:24.7	39.57	143.49	10	C	24	24	3.2	a	
A52	09 April (099) 1933	23:49:44.9	39.80	143.09	10	C	6	6	2.8	a	
A53	15 April (105) 1933	11:08:40.8	40.46	144.46	10	C	7	7	4.1	a	
A54	19 April (109) 1933	2:55:31.6	39.75	144.89	35	F	35	33	2.9	a	
A55	19 April (109) 1933	20:57:53.4	40.18	145.50	63	F	8	8	2.9		
A56	21 April (111) 1933	20:39:48.5	34.09	141.72	56	F	39	39	1.7		
A57	22 April (112) 1933	8:51:05.5	42.24	142.55	10	C	33	33	3.3	k	
A58	23 April (113) 1933	7:13:42.0	39.34	143.47	10	C	46	43	2.9	a	$6\frac{1}{4}$
A59	23 April (113) 1933	8:25:53.5	39.29	144.22	10	C	13	12	2.9	a	
A60	23 April (113) 1933	12:19:37.3	39.89	144.57	10	C	6	6	4.4	a	
A61	25 April (115) 1933	1:57:31.6	39.51	143.57	10	C	10	10	2.9	a	
A62	07 May (127) 1933	16:34:18.7	42.48	149.11	10	C	8	6	3.0		
A63	23 May (143) 1933	23:33:53.0	39.52	144.00	10	C	25	25	3.1	a	
A64	24 May (144) 1933	10:38:39.5	38.33	142.18	18	F	7	7	5.4	a	

Table 2. (*Continued.*)

Number *	Date D M (J) Y	Origin time GMT	Epicentre (°N)	(°E)	Depth (km)	Code†	Stations Read	Used	rms (s)	Focal mechanism††	Magnitude M_{PAS}
A65	05 June (156) 1933	1:51:20.3	36.48	141.05	10	C	35	35	2.2		
A66	08 June (159) 1933	18:10:40.4	40.17	144.80	10	C	100	98	2.3		$6\frac{1}{4}$
A67	12 June (163) 1933	21:08:16.8	39.01	142.37	10	C	71	68	3.1		
A68	13 June (164) 1933	20:33:43.1	41.00	142.94	53	F	102	99	2.6		$6\frac{1}{4}$
A69	17 June (168) 1933	14:01:49.0	41.19	144.21	10	C	25	24	4.6		
A70	18 June (169) 1933	21:37:38.4	38.32	142.07	34	F	160	154	3.0	T	7.3
A71	28 June (179) 1933	6:20:51.3	38.24	142.83	10	C	4	4	1.4		
A72	02 July (183) 1933	16:48:16.1	40.08	142.81	30	F	30	28	2.5		
A73	10 July (191) 1933	0:21:32.5	38.90	144.76	10	C	94	93	2.3		$6\frac{1}{4}$
A74	20 July (201) 1933	23:13:58.6	38.69	144.90	30	F	88	87	2.3		$6\frac{3}{4}$
A75	22 July (203) 1933	6:31:28.0	40.05	144.75	61	F	9	9	3.4		
A76	07 August (219) 1933	0:41:52.5	39.62	144.57	51	F	50	50	2.9		
A77	29 August (241) 1933	12:31:23.8	37.74	141.97	32	F	55	53	3.1		
A78	12 September (255) 1933	5:05:21.5	39.28	144.00	10	C	10	9	4.5		
A79	16 September (259) 1933	17:29:09.1	36.16	139.99	26	F	5	5	0.4		
A80	17 September (260) 1933	4:02:43.7	40.61	144.40	14	F	12	11	5.0		
A81	21 September (264) 1933	3:14:26.2	37.13	136.99	11	F	88	87	2.8		$6\frac{1}{4}$
A82	21 September (264) 1933	9:47:59.8	38.68	143.12	10	C	78	75	2.9		$6\frac{1}{4}$
A83	21 September (264) 1933	13:42:22.6	39.00	142.97	10	C	20	17	3.4		
A84	21 September (264) 1933	19:43:34.8	38.54	143.74	10	C	36	35	3.2		
A85	24 September (267) 1933	16:11:35.2	43.23	139.23	10	C	5	5	6.1		
A86	01 October (274) 1933	14:35:05.3	36.16	143.24	30	F	18	13	6.5		5.6
A87	02 October (275) 1933	3:33:22.3	36.34	141.71	9	F	11	10	5.0		
A88	11 October (284) 1933	13:57:44.3	38.05	141.83	10	C	73	67	4.7		
A89	23 October (296) 1933	0:41:32.0	39.98	144.08	3	F	10	9	6.4		
A90	01 November (305) 1933	8:21:49.9	35.33	141.10	10	C	15	11	4.9		
A91	07 November (311) 1933	16:59:14.5	35.40	140.90	10	C	12	9	6.4		
A92	08 November (312) 1933	5:44:01.2	41.20	142.64	10	C	45	41	4.8		
A93	27 November (331) 1933	7:50:02.0	36.41	141.63	10	C	10	9	3.3		
A94	27 November (331) 1933	19:14:20.7	39.46	143.69	10	C	55	50	4.7		

*F, foreshock; M, main shock; A, aftershock (genuine or not).
†Depth codes: C, constrained; F, floated.
††Focal mechanism codes: N, Normal faulting; T, thrust faulting; a, Anaseismic ('Compressional') at MIZ, presumed normal; k, Kataseismic ('Dilatational') at MIZ, presumed thrust.

upwards triangles as Centennial locations and inverted triangles as Uchida *et al.*'s (2016) solutions.

3 MAGNITUDES

Magnitudes assigned historically to the 1933 Sanriku earthquake have varied—and indeed grown regularly—with time. The earthquake was first given a magnitude of 8.3 by Gutenberg & Richter (1936), rounded to $8\frac{1}{4}$ in the first edition of *Seismicity of the Earth* (Gutenberg & Richter 1941), then a figure of 8.5 in the second, definitive edition (Gutenberg & Richter 1954) and an astounding magnitude of 8.9 by Richter (1958), which was retained into the National Geophysical Data Center database. Incidentally, this value of 8.9 is the largest magnitude ever assigned under the conventional scheme consisting of manually measuring amplitude traces, and before the use of a 'moment magnitude' scale M_w requiring in principle the genuine physical computation of a seismic moment.

Unfortunately, the original entry for the Showa Sanriku earthquake is missing from the available collection of B. Gutenberg's work pads (Goodstein *et al.* 1980), and it is thus impossible to assert beyond doubt the origin of the numbers proposed by B. Gutenberg and C.F. Richter. In their earliest estimate, Gutenberg & Richter (1936) apparently used a surface wave major passage (their so-called 'W_2'), for which any kind of distance correction must have been highly imprecise. A likely scenario is that their subsequent estimates ($8\frac{1}{4}$ and 8.5) were obtained mostly from body waves, and that the higher figure published later (8.9) resulted from an attempt to convert this body-wave magnitude into a 'unified' magnitude. In doing so, Richter (1958) would have tacitly assumed that the event was following the same scaling laws as the group of (presumably mostly interplate thrust) events that had been used to derive empirical relationships between body- and surface-wave magnitudes. As we will show, a considerable amount of evidence suggests that the 1933 event featured a fast, 'snappy' source, making it a violator of such scaling laws, and explaining the record-high magnitude value obtained by Richter (1958).

Kanamori (1971) personally reassessed a large data set of both body- and surface-wave magnitudes, and obtained values of M_s = 8.34, m_B = 8.16 (from *P* waves) and 8.22 (from *SH* waves); we note however that he compiled body-wave magnitudes at periods (7–14 s for *P* and 8–16 s for *S*) significantly longer than mandated for measuring a standard body-wave magnitude m_b under the Prague formula (Vaněk *et al.* 1962), hence the ascribed symbol m_B. It is highly probable that Gutenberg and Richter's (1941) essentially equivalent estimate ($8\frac{1}{4}$) was similarly obtained. By contrast, we have independently reassessed a genuine m_b from records at Pasadena (PAS) and Riverside (RVR), written on short-period Benioff seismometers (T_p = 0.5 s and T_g = 0.2 s), for which we have verified that the wave trains of maximum amplitude have periods in the vicinity of 1 s. A maximum measured amplitude of 2.3 cm on the

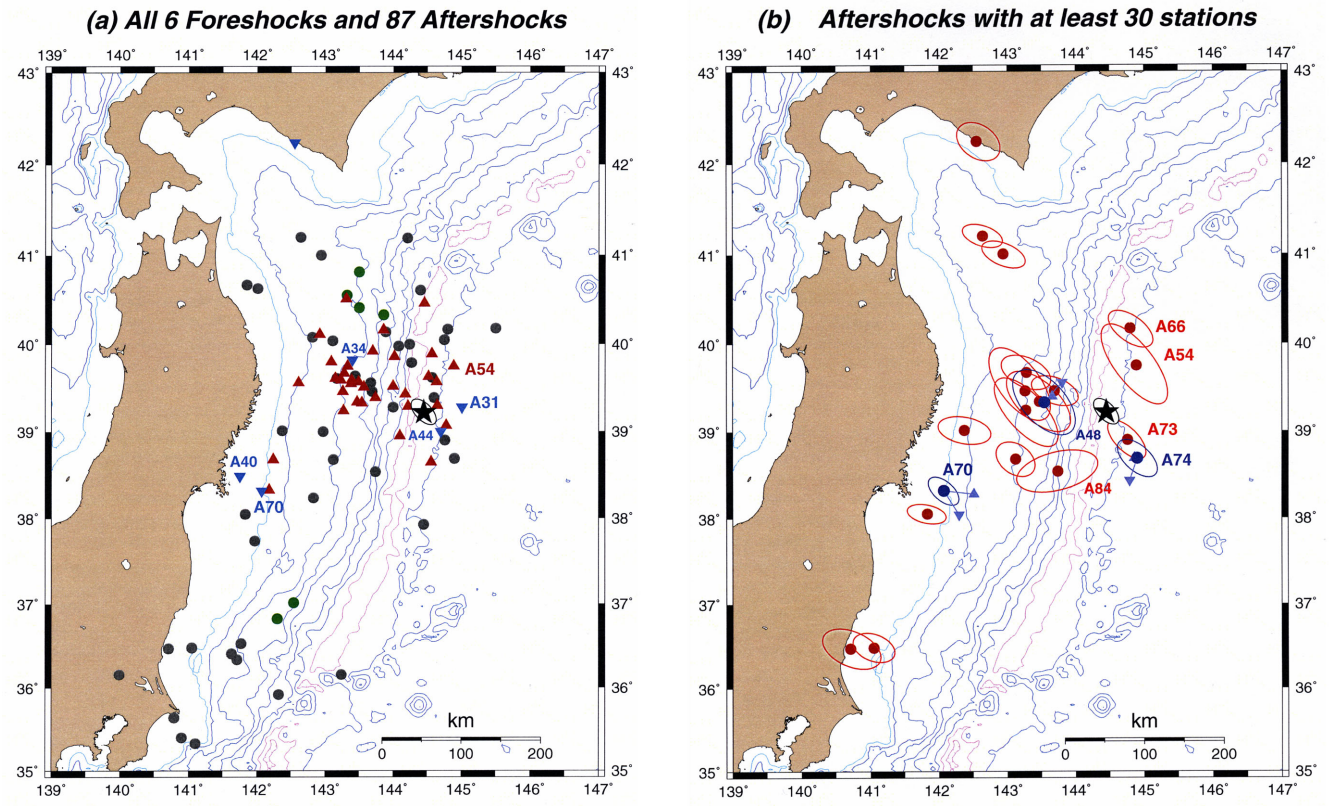

Figure 4. (a) Epicentres of six foreshocks (green) and 87 aftershocks relocated in this study. Isobaths as in Fig. 2(a). The black star (with Monte Carlo ellipse) shows the relocated main shock epicentre. The red triangles show those events whose first motions at MIZ are anaseismic (like the main shock, hence presumed normal faulting), the blue inverted triangles those with kataseismic first motions (presumed thrust) and the grey dots those without available or definitive first motions. Events described in the text are labeled. (b) Sub-dataset of Fig. 4(a) showing events whose relocated data sets contain more than 30 stations. Also shown are the relevant Monte Carlo ellipses indicating that these events are the better located ones. The five events relocating eastwards of the trench and considered to be genuine aftershocks are identified with a label cross-referenced to Table 2. Shown in blue are events relocated by Engdahl & Villaseñor (2002) (upward triangles), with Uchida *et al.*'s (2016) epicentres shown as inverted triangles. The main shock is shown as the black star.

PAS NS instrument leads to a magnitude $m_b = 7.6$ for an assumed maximum magnification of 80 000 (see discussion in Appendix A below). In turn, this figure can be used to propose a maximum gain of 30 000 for the vertical instrument at RVR, which recorded the shock with a maximum amplitude of 1.5 cm. Thus, our estimate of m_b, when correctly measured at 1 s is, as expected, significantly lower than m_B reported at much longer periods by Kanamori (1971), but much larger (by more than one unit) than the saturated value ($m_b = 6.0$) derived theoretically by Geller (1976) for m_b accurately measured at a period of 1 s. This latter remark indicates that the earthquake violates the scaling laws which control the saturation of m_b, as already noted and also discussed later in this paper.

3.1 Felt intensities

On Fig. 5, we show a map (a) of JMA intensity isoseismals compiled by Honda & Takehana (1933) and compare it with a database of 2011 Tohoku intensities (b) (Ishibe, personal communication, 2015). The two data sets are not directly comparable since the 2011 event was both closer to the coast of Japan, and hence to populated areas, and of larger moment than the Showa Sanriku earthquake. Furthermore, the only information available in Honda & Takehana (1933) consists of linear isoseismals, while a much more complete data set is available in 2011. Notwithstanding these reservations, we proceeded to compare the felt intensities of the two events as follows: first, we convert JMA intensities for the 2011 event to Modified Mercalli Intensities I_{MM}, using Wong & Trifunac's (1979) relation

$$I_{MM} = 2 \cdot I_{JMA} - 2.2 \qquad (1)$$

Then for each data point, we compute, as a function of an assumed magnitude M, an expected intensity $I_{Exp}(M)$ using Atkinson & Wald's (2007) eq. (1), which relates MMI values to earthquake magnitude M, and various geometrical factors, primarily hypocentral distance. We use their 'California' model, more representative of a tectonic environment than their 'Central & Eastern U.S.' one. We then define a residual $\mathrm{Res} = I_{MM} - I_{Exp}(M)$, and plot (in black) on Fig. 5(c) the value of the root mean square (rms) of the distribution of residuals Res at all locations, as a function of the magnitude M used to compute $I_{Exp}(M)$. Quite remarkably, the minimum of the rms residual is obtained for $M \approx 8.95$, which is in excellent agreement with the moment magnitude of the 2011 Tohoku earthquake. However, when repeating the experiment for the 1933 event (in red on Fig. 5c), the best fit is obtained for $M \approx 9.42$. We will show in Section 4 that this value is nearly one unit larger than the moment magnitude derived from mantle waves (or larger by a factor of 30 in terms of seismic moment).

In other words, the 1933 Sanriku earthquake generated felt intensities on the Japanese mainland which would have been more characteristic, under scaling laws, of a much larger earthquake. This again supports the model of an earthquake source anomalously rich in high frequencies, and thus violating seismic similitude laws.

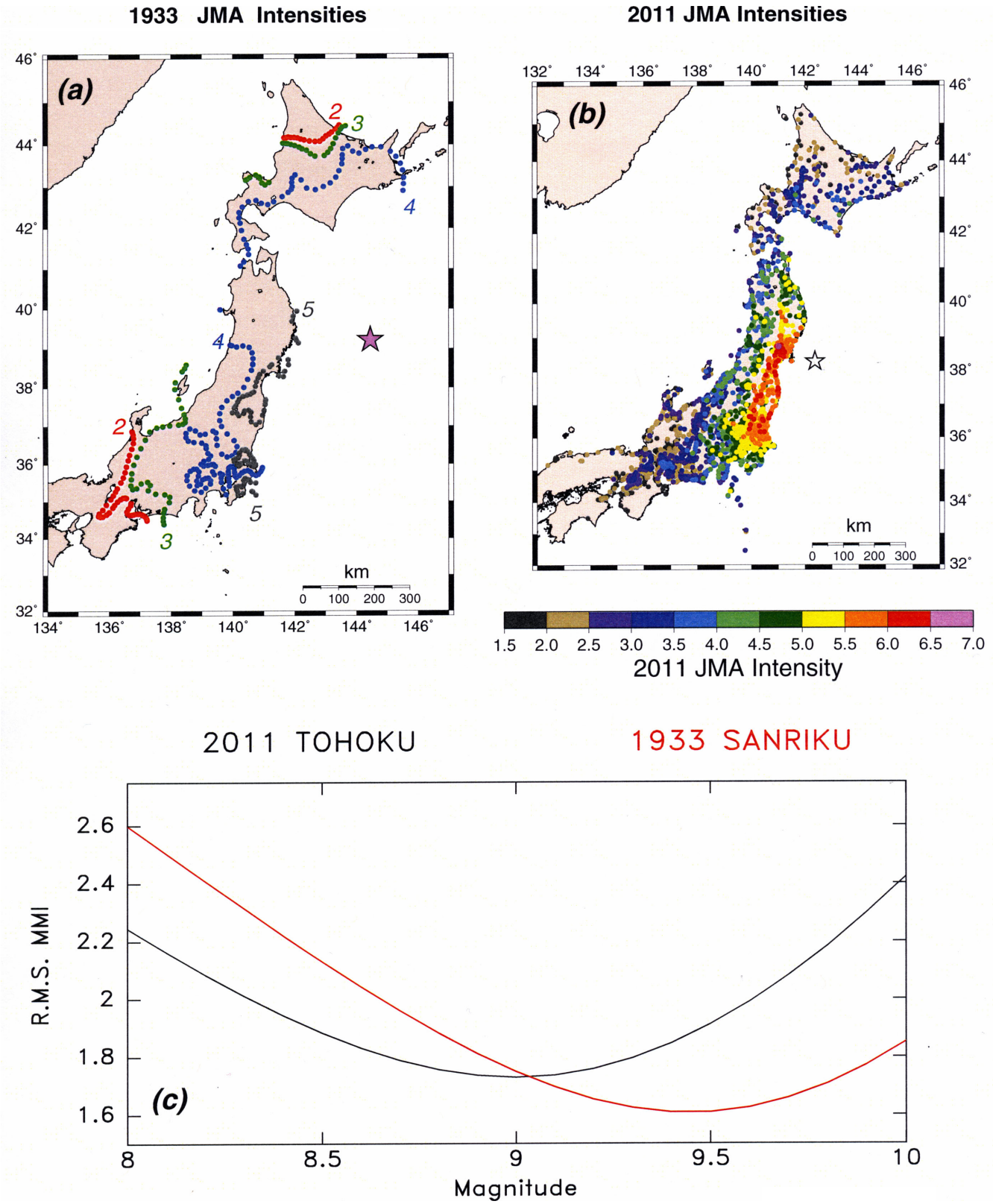

Figure 5. (a) Isoseismals of JMA intensities for the 1933 Sanriku earthquake, replotted from Honda & Takehana (1933). (b) Map of JMA intensity reports for the 2011 Tohoku event (Ishibe, personal communication, 2015). (c) Root-mean-square residuals of observed equivalent MMI intensities compared to values predicted using Atkinson & Wald's (2007) model, as a function of magnitude *M*, for the 2011 (black) and 1933 (red) earthquakes. Note that the best fit is correctly predicted for the former, but would require a significantly larger magnitude for 1933. See the text for details.

Table 3. List of stations used in the PDFM inversion.

Code	Station Location	Instrument	Distance (°)	Azimuth (°)	Phases used
CTO	Cape Town, South Africa	Milne-Shaw	136.9	260.0	G_1, R_1
HUA	Huancayo, Peru	Wenner	135.6	63.0	G_3
RIV	Riverview, Australia	Wiechert	73.1	174.2	G_1, R_1
UPP	Uppsala, Sweden	Wiechert	71.9	334.9	G_1, R_1

4 FOCAL MECHANISM AND STATIC MOMENT

4.1 Main shock

Matuzawa (1942) first compiled *P*-wave first-motion polarities at worldwide stations, pointing out to systematic kataseismic arrivals ('dilatational', or towards the source) in the far field, and anaseismic ones ('compressional', or away from the source) at short distances. He went on to correctly describe the geometry of the released stresses, but of course his study predates the double-couple concept for the seismic source, and thus he could not derive a proper mechanism, since he sought only a single fault plane separating dilatational and compressional arrivals.

Kanamori (1971) complemented Matuzawa's data set with additional readings and *S*-wave polarities, and proposed a pure normal-faulting focal geometry: $\phi = 180°$, $\delta = 45°$, $\lambda = -90°$, these round numbers suggesting an approximate solution. Using this mechanism, he derived a seismic moment of 4.3×10^{28} dyn cm from a data set of 13 spectral amplitudes of 100-s surface waves. Ben-Menahem (1977) used PAS strainmeter spectral amplitudes at 200 s to infer a potency of 276 km^3, equivalent to $M_0 = 1.4 \times 10^{29}$ dyn cm. Okal (1992) used a Wiechert record at Uppsala and multiple passages of Love and Rayleigh waves on Benioff's (1935) prototype strainmeter at PAS to obtain spectral amplitudes at longer periods (reaching 250 s), and estimated a moment of 9.5×10^{28} dyn cm at those periods.

Here, we invert the moment tensor using the preliminary determination of focal mechanism (PDFM) method, introduced by Reymond & Okal (2000). Based on an idea from Romanowicz & Suárez (1983), it consists of inverting only the spectral amplitudes of mantle waves, while discarding the phase information. As shown by Okal & Reymond (2003), it is particularly well suited to historical seismograms for which timing and epicentral imprecision can strongly affect spectral phases, while leaving the amplitudes unaltered. The method, which can work with as few as three stations, suffers from a double indeterminacy of ±180° on both the strike and slip angles, which can usually be resolved with the knowledge of a few *P*-wave first-motion polarities.

A list of records used in this study is given in Table 3. To guard against possible remaining uncertainties regarding their responses during the development stages of the instrument, we eliminated the PAS strainmeter records. Given the size of the earthquake, we allow a component of directivity, and find that a southward-propagating rupture improves the quality of fit by about 15 per cent; the final solution converges to $\phi = 200°$ (or 20°), $\delta = 61°$, $\lambda = 271°$ (or 91°), with a scalar moment $M_0 = (6.0 \pm 0.9) \times 10^{28}$ dyn cm (Fig. 6). The normal-faulting character of the event, well established by the data sets compiled by Matuzawa (1942) and Kanamori (1971), removes the indeterminacy on λ, and we prefer $\phi = 200°$, which remains compatible with the overwhelming majority of the first-motion data set (Fig. 7). Our solution is rotated only 25° from Kanamori's (1971) in the formalism of

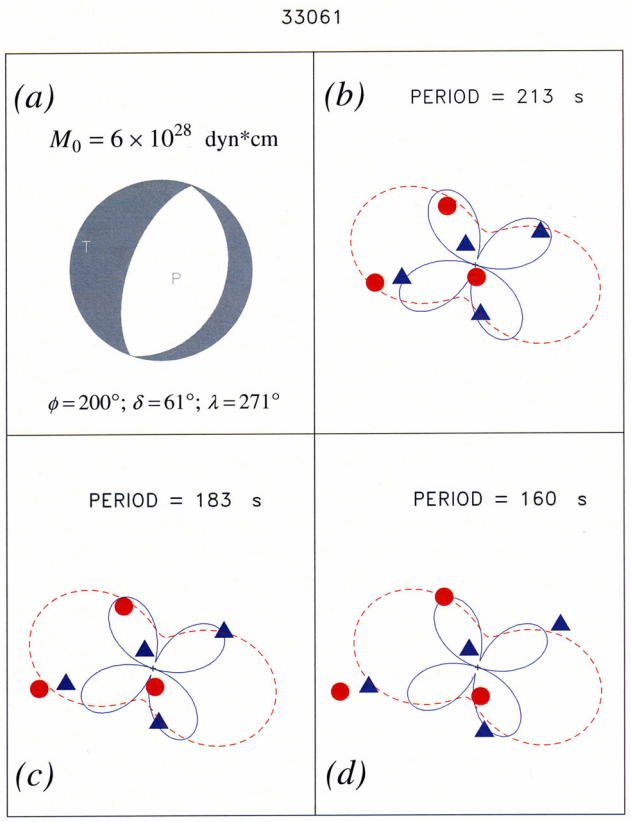

Figure 6. Results of PDFM inversion. (a) Inverted focal mechanism and seismic moment. (b)–(d) Fits to radiation patterns at representative periods. The continuous traces are the theoretical spectral amplitudes as a function of azimuth (Love: solid, blue and Rayleigh: dashed, red) and the individual symbols the amplitudes observed at the stations (Love: blue triangles and Rayleigh, solid circles). Scales are arbitrary, but common to all plots within a period box.

Kagan (1991), and strikes parallel to the NNW trend of the Japan Trench and to fault scarps on the inner trench slope in the epicentral area.

An independent estimate of the moment of the 1933 main shock was recently obtained by Kanamori (personal communication, 2012), based on the exclusive use of the PAS strainmeter records. In this respect, this study and Kanamori's are complementary in that they use independent data sets and different methods: Kanamori's study is based on scaling the source to that of a modern event recorded in a similar source–receiver geometry (Kanamori *et al.* 2010); it yields a seismic moment of $(8 \pm 1) \times 10^{28}$ dyn cm, in the geometry of Kanamori (1971).

While Kanamori's investigation features a more complete analysis of the effects of directivity (including the possibility of a bilateral rupture) and source depth, we propose a slightly rotated mechanism, which would in general trade-off with scalar moment

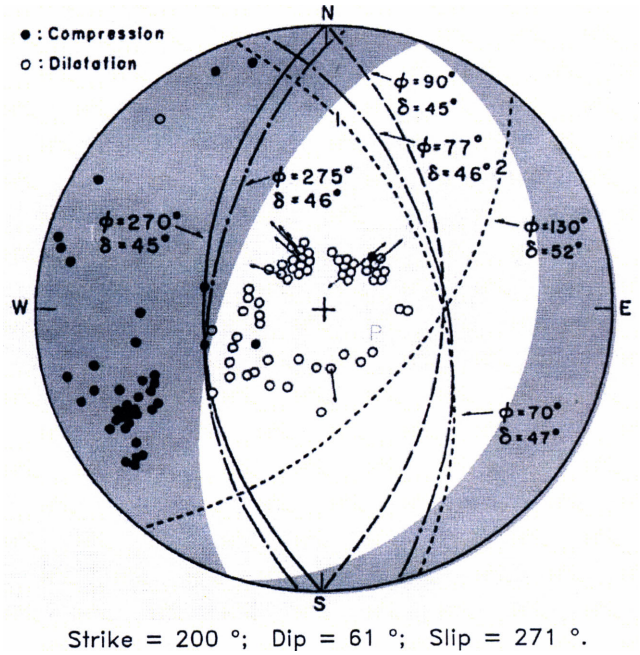

Figure 7. Preferred PDFM-inverted focal mechanism superimposed on fig. 4 of Kanamori (1971), emphasizing our solution's excellent fit to that study's original data set. Note that the azimuths listed by Kanamori (1971) are dip directions, 90° greater than fault strike under the conventions utilized here, which are the standard ones used in the Global CMT project, as defined originally by Kanamori & Cipar (1974).

(and explain lower values of M_0). Notwithstanding these differences of methodology, the comparison of our results with Kanamori's (personal communication, 2012) would suggest as a consensus a one-significant-digit value of $M_0 = 7 \times 10^{28}$ dyn cm ($M_w = 8.5$), larger than proposed by Kanamori (1971), but falling short of Ben-Menahem's (1977) substantially larger inferred moment.

At this stage, it is interesting to discuss Matuzawa's (1942) solution in the context of our modern focal mechanism. This author described the source under the so-called conical model ('Kegel-Typus'), in which compressional and dilatational rays are separated at the focus by a cone with a 45° semi-apex angle. On Fig. 8, we present a Mercator projection analogous to his Fig. 1 on which we have reproduced (in blue) the nodal line representing the locus of emergence of rays departing on the cone. We superimpose (in red) the corresponding loci of nodal stations for our mechanism. The individual green triangles are the stations available to Matuzawa, compiled from his two papers on earthquake location and focal mechanism (Matuzawa 1935, 1942). As shown on Fig. 8, the two models (conical and double-couple) predict opposite ground motions in two broad regions of the Earth: Southwestern China and Eastern Turkestan; and the Arctic, including Eastern Siberia, Kamchatka, the Aleutians, Alaska and the Yukon. Note that only four stations among Matuzawa's data set sample these regions; they are shown as inverted triangles on Fig. 8: Sitka (SIT), whose arrivals he labels with question marks, Zi-ka-wei (ZKW) and Nanjing (NJI), which he describes as emergent, and Chichi-jima (CBI) in the Bonin Islands, which Matuzawa (1942) reports as part of the compressional Japanese stations, but which is absent from the data set plotted by Kanamori (1971). Note that in 1933, there were no stations other than SIT in Alaska (College started in 1935). On the other hand, the two mechanisms predict identical polarities at all other stations, including the large groups in Japan (anaseismic), Europe and North America (kataseismic).

We were able to inspect scans of the original records available to T. Matuzawa, which are preserved at Tohoku University. The SIT record clearly shows an impulsive kataseismic (to north and west) arrival, and that at ZKW a small, but clear, anaseismic (to west) one, both polarities being in agreement with our double-couple solution. The record at Nanjing shows a very weak, emergent westward (anaseismic) first motion, again in agreement with our mechanism. We were unable to find a copy of the record at CBI. In this respect, we must conclude that Matuzawa's (1942) preference for the 'conical model' (and his intriguing rejection of the 'quadrant model', an early forerunner of the double-couple) probably stems from the unfortunate geographical bias in his data set, and his unexplained misinterpretation of the SIT and ZKW records.

4.2 Uchida *et al.*'s composite solution

In a companion paper, Uchida *et al.* (2016) have argued for a composite source of the 1933 event, based on a discrepancy between *P*-wave first-motion constraints and the observed initial polarity of tsunami waves recorded on the Sanriku coast of Japan, the latter being consistently observed as an initial inundation (upwards displacement of the sea level). In simple terms, and for a dip-slip motion on an inclined fault striking parallel to the beach, the polarity of initial tsunami motion at a local shore is a subtle combination of three factors: (i) the nature of faulting (thrust or normal); (ii) the direction of dipping of the fault (landwards or seawards) and (iii) the dip angle δ of the fault. It has been systematically observed (e.g. Borrero *et al.* 1997) and theoretically explained (Tadepalli & Synolakis 1996; Okal 2008) that in the classical case of a shallow-dipping subduction interplate thrust earthquake, the tsunami features an initial recess at the local beach on the overriding plate. In the case of the 1933 mechanism shown on Fig. 7, the normal-faulting polarity should reverse this trend, but the steep dip angle ($\delta = 61°$) returns the tsunami first motion to a predicted initial recess, which disagrees with the observations.

To alleviate this discrepancy, Uchida *et al.* (2016) have proposed a composite model, consisting of an initial (primary) rupture generally similar in location and geometry to our model on Figs 2 and 7 (i.e. on a steep landward-dipping fault), followed by a secondary source featuring normal faulting on a plane striking along the same direction, but dipping oceanwards at an angle of 45°, and displaced 50 km to the west of the primary source. While not specifically given by Uchida *et al.* (2016), the time lag between the two sources would be long enough that all *P*-wave first motions will be related to the primary source, but would remain significantly shorter than the travel time of the tsunami between the two sources, estimated at 200 s. As such, the initial polarity of the tsunami on the Sanriku beaches will be controlled by the closest source, namely, the secondary one. Finally, the existence and geometry of the secondary source is supported by the identification of a small group of aftershocks along its proposed fault plane (Uchida *et al.* 2016).

In terms of mantle wave excitation, and given a sufficiently short time lag between the two sources, their combination will behave as the sum of their moment tensors. Because the two sources share their null axis, they combine into a pure double-couple (see Appendix B), and since the secondary source is close to the primary's conjugate solution, the combined double-couple will be rotated only a few degrees (in the sense of Kagan 1991) from the primary solution. In practical terms, the combined solution will remain in agreement with the results of our PDFM inversion. We also show in Section 6 that the composite source is compatible with the main

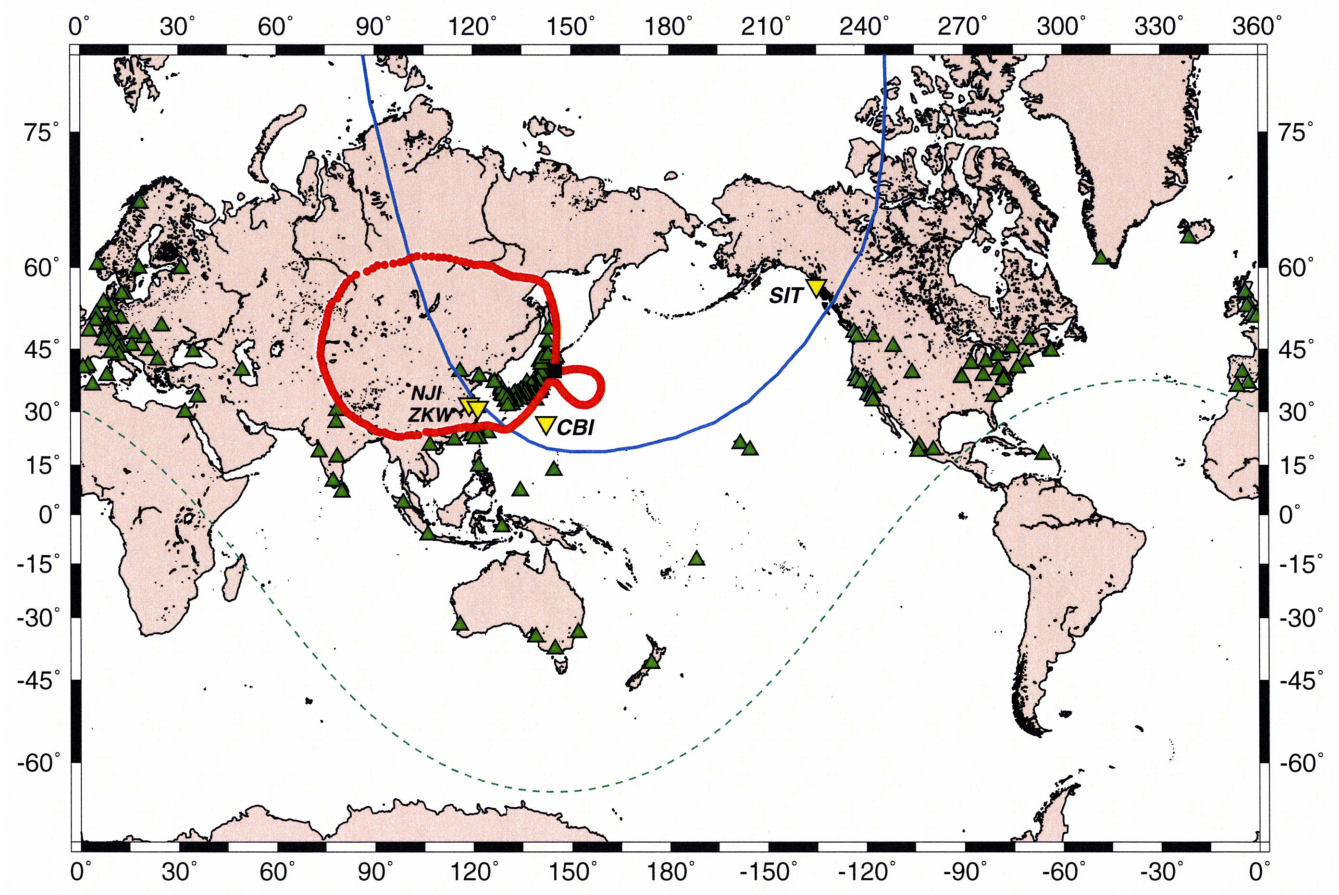

Figure 8. Distribution of first motion polarities of the Showa Sanriku earthquake. This Mercator projection complements Matuzawa's (1942; fig. 1). The blue line reproduces his nodal line ('Knotenlinie'), separating compressional and dilatational arrivals under his 'conical model'. The lines of red dots similarly separate compressional and dilatational arrivals under the double-couple solution obtained in this study. The small green triangles are the stations used by Matuzawa (1942), and the four larger inverted triangles those stations (with codes) for which the two models predict opposite polarities. The dashed green line represents the boundary of the core shadow, 102.6° from the source.

characteristics of the far-field tsunami as observed in the Hawaiian Islands.

4.3 Main aftershock, Event A70

With a published PAS magnitude of 7.3, Event A70 (1933 June 18, 21:37 GMT) is by far the largest aftershock in the series. Fig. 9(a) shows a focal mechanism compiled on the basis of seven first motion polarities read as part of this study (large symbols), and 44 transcribed from the ISS (small symbols). The event clearly features a thrusting mechanism ($\phi = 168°$, $\delta = 12°$ and $\lambda = 60°$). While poorly constrained, our floating depth relocation estimate converges on 34 km, while Uchida *et al.* (2016) propose a somewhat intriguing value of only 3 km. The Centennial catalogue uses a constrained depth of 35 km (Engdahl & Villaseñor 2002). Fig. 9(b) shows a cross-section of recent seismicity suggesting that this event could represent slip at the subduction interface, possibly triggered by stress transfer from the main shock. An analysis of the spectral amplitudes of Rayleigh and Love waves at De Bilt, Tucson and Honolulu yields a moment of 9.6×10^{26} dyn cm in the focal geometry of Fig. 9(a). The earthquake generated a minor tsunami with a maximum run-up of 9 cm on the Tohoku coast (Solov'ev & Go 1984).

4.4 Other events

The other aftershocks are in general too small to warrant a focal mechanism study. However, we examined systematically the records of aftershocks A08–A64 on the east–west component (mostly radial) of the Omori seismometer at Mizusawa (MIZ), whose scans are available at Tohoku University. When their polarity could be read in a definitive way, it is reported in Table 2; this allows a preliminary classification of the events as either compatible with the main shock, and thus presumed normal faulting, or of the opposite polarity, and thus possibly thrust faulting. The map on Fig. 4(a) has been keyed accordingly.

On Fig. 4(a), we note that the distribution of focal mechanisms does not correlate directly with the location of the events with respect to the trench interface: although seven presumed normal-faulting events are indeed located eastwards of the trench suggesting that they are genuine aftershocks (sharing fault plane and mechanism), two similarly located events (A31 and A44) have an incompatible mechanism; while they are smaller, arguably poorly located, events, it is worth noting that A31's depth converges to 49 km, and it could thus represent a compressional release upon bending in the deeper part of the plate (Chen & Forsyth 1978; Chapple & Forsyth 1979).

The situation is similarly mixed arcwards of the trench, with a group of about 20 presumed normal-faulting events (and one

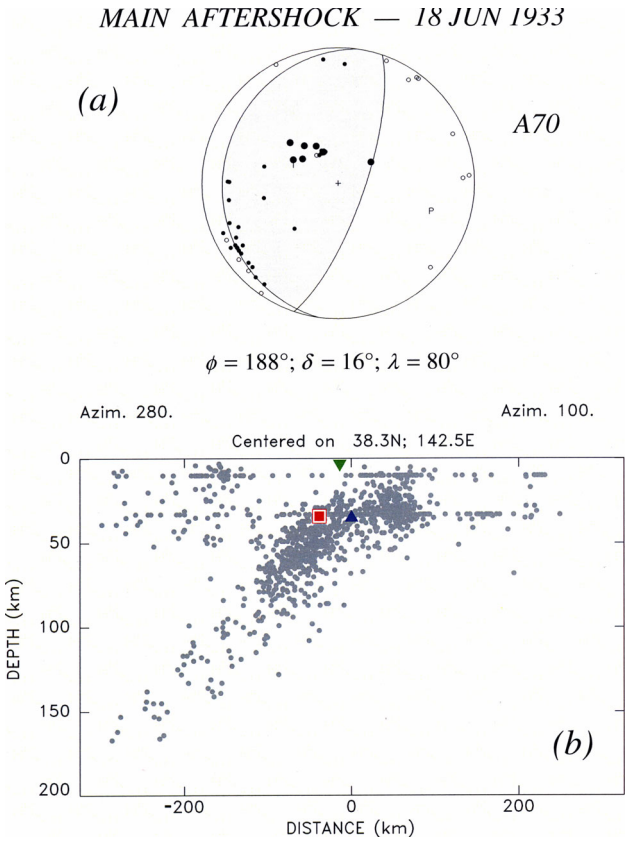

Figure 9. Focal mechanism of the main aftershock (A70). Larger symbols correspond to stations read as part of this study, smaller ones to polarities reported in the ISS. Shaded quadrants and solid symbols are compressional (anaseismic), open ones dilatational (kataseismic). (b) Hypocentral locations of Event A70 superimposed on a cross-section of seismicity along a 2.5° latitudinal band in its vicinity (epicentres are from the NEIC catalogue from 1970 to 2011, February, with at least one magnitude ≥4.5). The red bull's eye square is our preferred solution, the blue triangle the Centennial one (Engdahl & Villaseñor 2002) and the green inverted triangle Uchida *et al.*'s (2016). Vertical exaggeration: 2. This plot suggests that A70 could be an interplate thrust event.

presumed thrust, A34) forming a cluster centred about 100 km WNW of the main shock. These aftershocks probably released stresses transferred by the main shock into a system of normal faults documented in the upper plate above the slab interface (Gamage *et al.* 2009; Buck *et al.* 2015). It is worth noting that the GlobalCMT project lists no fewer than 18 normal-faulting aftershocks of the 2011 Tohoku mega-thrust event in the same area.

5 BODY-WAVE ENERGY AND SLOWNESS PARAMETER Θ

In order to further investigate the distribution of radiated energy across the frequency spectrum of the earthquake source, we compute the energy-to-moment ratio, characterized by the slowness parameter $\Theta = \log_{10} \frac{E^E}{M_0}$ introduced by Newman & Okal (1998), following the work of Boatwright & Choy (1986). We recall that scaling laws predict a theoretical value of $\Theta = -4.90$, shown as the grey diagonal on Fig. 10, adapted from Okal *et al.* (2012), and well upheld by a background data set of ∼90 recent earthquakes (solid dots). By contrast, earthquakes featuring a slow source, such as the so-called 'tsunami earthquakes' (Kanamori 1972), feature a value of Θ systematically deficient by more than 1 logarithmic

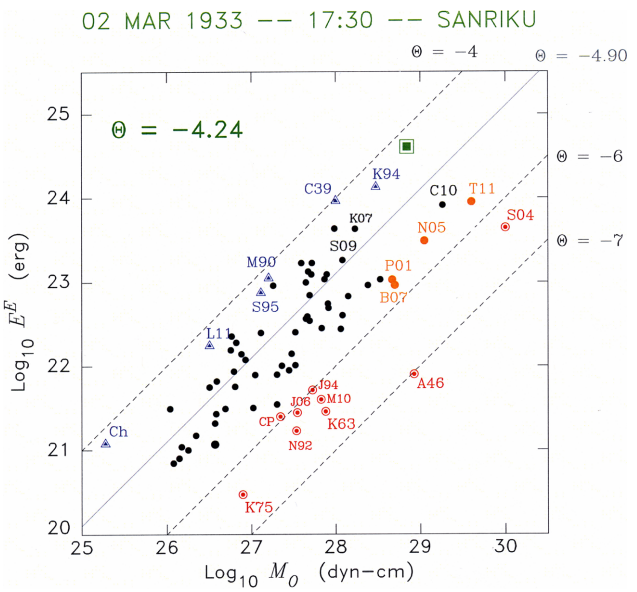

Figure 10. Estimated energy E^E versus moment M_0 for a background of large earthquakes of the past 35 yr. Lines of constant Θ are shown as dashed lines, with the solid grey line representing the theoretical value (−4.90) expected from scaling laws. The 1933 Sanriku event is shown as the large square symbol. The circular bull's eyes identify the 'tsunami earthquakes' with $\Theta < -5.80$. By contrast, the triangles identify 'snappy' earthquakes with $\Theta > -4.3$. Relevant earthquakes are identified as: A46, Unimak 1946; B07, Bengkulu 2007; C39, Chillán, Chile 1939; C10, Maule, Chile 2010; Ch, Christchurch 2011; CP, Chimbote, Peru 1996; J94, Java 1994; J06, Java 2006; K63, Kuril 1963 (20 Oct.); K75, Kuril 1975; K94, Kuril 1994; K07, Kuril 2007; L11, Loyalty Is. 2011; M90, Marianas 1990; M10; Mentawai 2010; N05, Nias 2005; N92, Nicaragua 1992; P01, Peru 2001; S95, Samoa 1995; S04, Sumatra 2004; S09, Samoa 2009 and T11, Tohoku 2011.

unit (bull's eyes on fig. 10; Newman & Okal 1998), while many intraplate events feature higher values of Θ (triangles on Fig. 10), which express larger stress drops (Choy *et al.* 2001; Okal & Kirby 2002; Choy & Kirby 2004).

To compute the energy radiated by the 1933 earthquake, we use three generalized *P*-wave records written in Southern California on the short-period seismometers which were then being developed by Benioff (1932). Appendix A details our estimation of adequate instrument constants for these instruments. In view of their rapidly falling response at periods as short as 5 s, we adapt slightly Newman & Okal's (1998) algorithm by integrating the spectrum between 0.2 and 3.3 Hz. The resulting parameters are $\Theta = -3.89$ at PAS, -4.52 at RVR and -4.19 at Mount Wilson (MWC). In addition, we use the EW Wood–Anderson torsion seismograph record at Santa Barbara (SBC), which, of course, features a much smaller amplitude, but whose response characteristics are much more robust (and as such they were the reference instruments used by Richter (1935) in his development of the magnitude concept). At SBC, we find $\Theta = -4.35$, with the average of the four estimates being $\Theta = -4.24 \pm 0.23$, a significantly larger value than theoretically predicted (-4.90) and generally observed for large interplate earthquakes (typically in the -5.4 range; orange dots on Fig. 10). On the other hand, our results are similar to those for many 'snappy' intraplate earthquakes featuring higher stress drops, such as the 1939 Chillán event (Okal & Kirby 2002) or the much smaller 2011 Christchurch earthquake. However, among the outer rise events listed in Table 1, the other recent shocks (2009 Samoa and 2007 Kuril) would exhibit no more than a trend towards enhanced Θ. Finally, we note that the

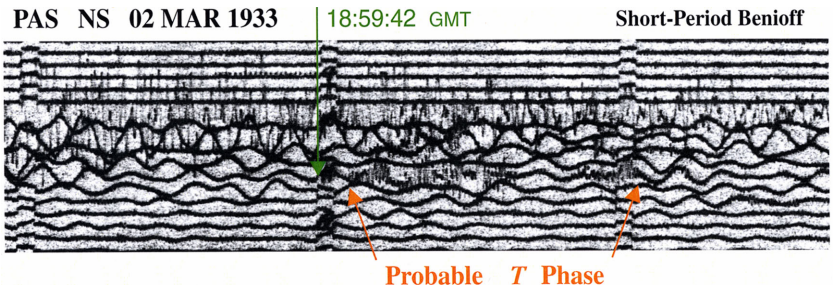

Figure 11. Close-up of the north–south short-period Benioff seismogram at Pasadena, showing the probable *T*-phase arrival. The time correction (–18 s) for the nearby minute mark was computed using the *P* arrival (not shown), as reported to the ISS. There are four lines to the hour.

average estimated energy of the 1933 earthquake, 4×10^{24} erg, is the largest value ever computed using Newman & Okal's (1998) algorithm. This is in line with our remark, in Section 3, that the earthquake was also given the largest ever magnitude (8.9) assigned empirically (before the formal computation of a seismic moment) by Richter (1958), presumably from a body-wave measurement, corrected using scaling laws that the earthquake actually violated.

5.1 The *T* wave at Pasadena

A remarkable high-frequency wave train is present on the PAS short-period Benioff seismogram starting at 18:59:50 GMT on 1933 March 2 (Fig. 11). Its duration (60 s) is too long for a local earthquake and no large aftershocks are known whose *P* wave would arrive at that time (Table 2). Rather, we propose that this signal represents a teleseismic *T* wave from the Sanriku main shock. This interpretation remains tentative since it is peaked around 2 Hz, which represents a lowermost frequency bound for propagation of a *T* phase in the SOFAR channel.

As expected, this signal is absent from torsion seismograms at all available Northern and Southern California stations (e.g. Berkeley, Santa Barbara and La Jolla). To our knowledge, the only stations other than PAS which at the time operated Benioff short-period instruments with very short galvanometer periods (0.2 s) were RVR, Tinemaha (TIN) and MWC, the latter only 13 km from PAS, but in a different geological context. Despite the much lower gain at which RVR is believed to have been operating (see Appendix A), a weak signal can be detected, which shares timing and duration characteristics with that at PAS, ruling out the latter's interpretation as some form of local noise. Traces may also be present at TIN (300 km from the nearest shore) around 19:00 GMT. At MWC, and following the passage of the main seismic phases, subsequent traces appear thickened on the record, probably due to systematic noise in the electrical circuits of the galvanometer; this obscures the seismogram to the extent that the presence or absence of a *T*-wave signal cannot be asserted.

The recording of a *T* wave at PAS, and probably at RVR, is remarkable, since the location of the stations is far from favourable (being 50 and 63 km inland, respectively). In particular, no *T* waves could be identified (even on spectrograms) at PAS, TIN and RVR following the 2011 Tohoku earthquake (we note, however, that the Pasadena station was moved 2.9 km from its original site (PAS) in 2006, in principle to a comparable site (PASC), but this may still affect the reception of high-frequency waves). By contrast, *T* waves are clearly extracted on a spectrogram of the 2011 Tohoku record at MWC, and, incidentally, as far inland as Isabella (ISA, 175 km from the nearest shore), but neither at TIN nor RVR. Based on a cross-correlation of 2011 *T*-waveform envelopes at MWC and at the Central California station HASF, located near a steep conversion slope and where the *T* arrival is impulsive, we define a 2011 arrival time of 07:18:56 at MWC. Assuming comparable conversions at the source and receivers, and taking into account an epicentral distance shorter by 207 km in 1933, we derive an expected arrival time of 19:01:08 at MWC for the 1933 Sanriku *T* phase. This is within 70 s of the arrivals on the 1933 record at PAS shown on Fig. 11, and only 50 s from the maximum of the proposed *T* phase, this time interval possibly reflecting a difference in source-side conversion between 1933 and 2011. We conclude that the signal shown on Fig. 11 is indeed a record of the *T* wave from the 1933 main shock. Unfortunately, because of the absence of other high-frequency seismic stations in the Pacific Basin in 1933, we could not confirm this interpretation.

We further quantify this 1933 *T*-wave arrival using the concept of *T*-phase energy flux (TPEF), introduced by Okal *et al.* (2003). As reviewed by Okal (2007), this algorithm consists of integrating (in the frequency domain) the kinetic energy of the *T* phase in a way reminiscent of the computation of radiated energy from body waves (Boatwright & Choy 1986; Newman & Okal 1998). When scaled to the seismic moment, it provides a proxy for earthquake source processes upholding or violating seismic scaling laws. Because of the effect of specific conversion parameters, whose influence becomes critical at the high-frequencies characteristic of *T* phases, this approach should not be used in an absolute way, but rather is limited to the comparison, at the same receiver and under comparable geometries, of relative values of TPEF and its ratio to M_0.

In the present case, we start by quantifying the 2011 Tohoku *T* phase at MWC, obtaining TPEF $= 1.6 \times 10^{-3}$ erg cm^{-2}. We note however that the record is noisy, and compute a value of 1.2×10^{-3} erg cm^{-2} for a comparable window of noise 15 min prior to the arrival, suggesting a contribution of only 4×10^{-4} erg cm^{-2} from the *T* phase itself. This would correspond to a parameter $\gamma = \log_{10} \frac{\mathrm{TPEF}}{M_0} + 30 = -3$ (Okal 2007), given the seismic moment $M_0 = 4 \times 10^{29}$ dyn cm of the 2011 Tohoku earthquake. In the case of the 1933 event, we were able to digitize a scanned copy of the 1933 *T* phase at PAS. Assuming instrument constants $T_p = 0.5$ s, $T_g = 0.2$ s and a gain of 80 000 (see Appendix A), we obtain TPEF $= 3.5 \times 10^{-2}$ erg cm^{-2}, leading to $\gamma = -0.3$ for $M_0 = 7 \times 10^{28}$ dyn cm. In short, the 1933 earthquake excited *T* phase energy 500 times more efficiently than the 2011 Tohoku event. This supports the concept of a seismic source spectrum particularly rich in high frequencies. By comparison, a difference $\gamma_{2007} - \gamma_{2006} = 0.8$ logarithmic units (or a ratio of 6) was found for *T* phases recorded at Midway Island from the two Kuril events of 2006 November 15 (interplate thrust) and 2007 January 13 (off-trench normal faulting).

In conclusion, a large body of evidence proves that the Showa Sanriku earthquake featured a rapid or 'snappy' source, very

significantly enriched in higher frequencies. Beyond the exceptionally high value of its estimated energy and the corresponding Θ parameter, this includes high felt intensities, exceptionally large high-frequency magnitudes and the generation of a significant *T* phase. While these characteristics are generally commonly observed during modern intraplate events (Choy & Kirby 2004), the mere size of the 1933 event results in a few unparalleled observations. Incidentally, we note that the high-frequency 'blue' character of the spectrum of the Showa Sanriku earthquake was already noted by Brune & Engen (1969) who noted deficient Love spectral amplitudes at 100 s, with respect to Richter's (1958) estimate of $M = 8.9$, and concluded that *'the very long-period excitation by this earthquake was relatively small'*.

6 FAR-FIELD TSUNAMI

The 1933 Sanriku earthquake generated a powerful tsunami which killed over 3000 people on the coastlines of Eastern Honshu. While this death toll is dwarfed by that of the catastrophic 2011 Tohoku event, the 1933 tsunami was the third deadliest in the 20th century, after the 1952 Kamchatka and 1976 Mindanao disasters, and produced run-up reaching 29 m in Yamada Bay, Iwate Prefecture (Ishimoto 1933; Iida *et al.* 1967), comparable in range to many observations in 2011, and certainly considerably higher than the standard of 6 m apparently adopted later throughout Japan for the building of protective tsunami walls (Fukuchi & Mitsuhashi 1983). As mentioned in the prologue, the tsunami caused significant damage on the Big Island of Hawaii; while recorded on tide gauges, it had no notable effects along the U.S. West Coast. In this respect, among the earthquakes listed in Table 1, the 1933 Sanriku event is the only one which exported destruction several thousand kilometres into the far field, thus serving a unique proof that outer slope normal-faulting events do contribute to tsunami hazard in the far field, and should therefore be taken into account in relevant tsunami hazard assessments.

In this context, this section describes a number of numerical simulations of the effects of the tsunami in the far field, based on several source models, including variations of the composite source proposed by Uchida *et al.* (2016). The observable data lending themselves to modeling consist of the following:

(i) The maregram reproduced on Fig. 12(a), recorded at Honolulu and published as part of the Special Report of the Earthquake Research Institute (Anonymous 1934). Fig. 12(b) shows a close-up of an eight-hour window, digitized from *(a)* and band-pass filtered between 0.1 and 3 mHz. Note the strongly impulsive initial down-draw upon arrival of the first wave around 14:40 HST (01:10 GMT on March 3).

(ii) Run-up values reported on the west coast of the Big Island of Hawaii and compiled as part of the NOAA digital tsunami database (http://www.ngdc.noaa.gov/hazard/tsu_db.shtml), namely 3.20 m at Keauhou, 3.0 m at Kailua-Kona and 2.90 m at Napoopoo. Additional run-up data (less than 1 m on Maui and Oahu and 10 cm in California) are generally too small to be meaningfully modeled.

Our goal here is to verify that a model compatible with our seismological investigations, including the composite source proposed by Uchida *et al.* (2016), can explain the damage wrought by the tsunami on the Big Island, a unique occurrence in the far field for a normal-faulting intraplate earthquake.

Our simulations use the MOST algorithm (Titov & Synolakis 1998), which solves the full non-linear equations of hydrodynamics under the shallow-water approximation, by finite differences and through the method of alternate steps (Godunov 1959). MOST has

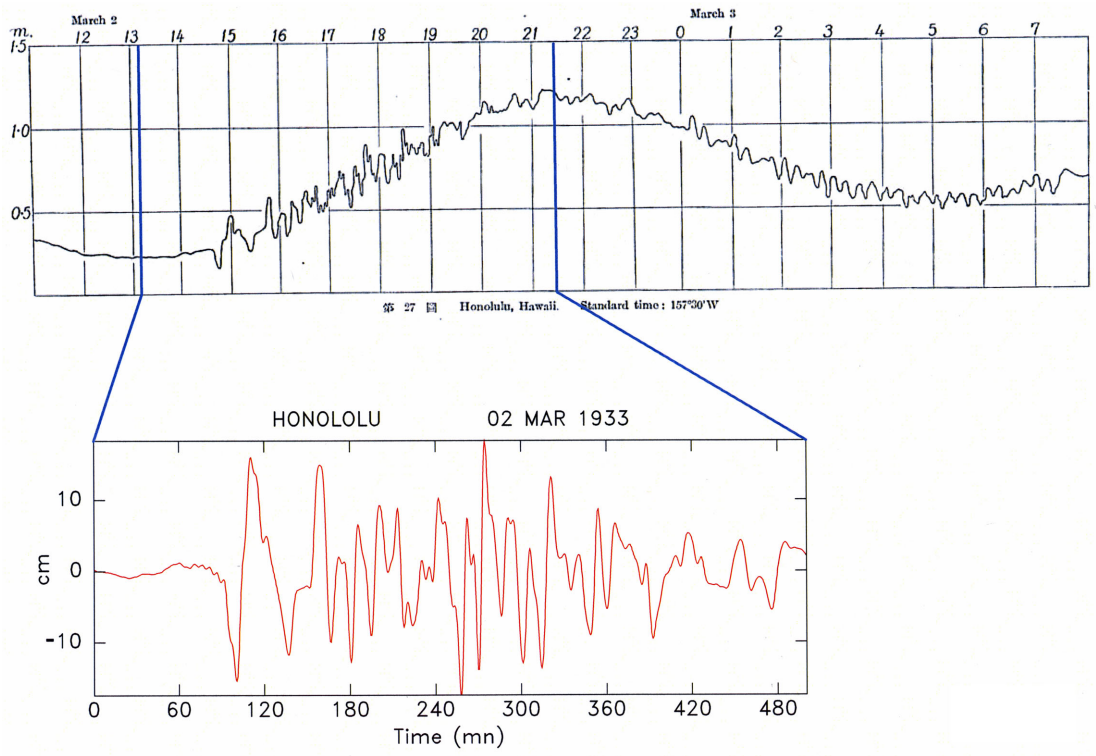

Figure 12. Top: maregram of the 1933 tsunami recorded in Honolulu, reproduced from Anonymous (1934). Bottom: excerpt from maregram (between 13:10 and 21:30 HST), filtered between 300 and 10 000 s. Note sharp initial down-draw, consistent with normal-faulting mechanism.

Table 4. Sources parameters used in tsunami simulations.

Name	Focal mechanism			Source parameters			Moment	Centroid	
	ϕ (°)	δ (°)	λ (°)	Length (km)	Width (km)	Slip (m)	(10^{28} dyn cm)	(°N)	(°E)
Primary mechanisms									
A1	200	61	271	170	33	18.5	7	39.22	144.45
A2	200	61	271	100	35	30.0	7	39.22	144.45
A3	200	61	271	100	35	30.0	7	39.67	144.55
A4	200	61	271	100	35	30.0	7	38.77	144.35
Secondary mechanisms									
U1	18	45	268	100	35	30.0	7	39.37	143.91
U2	18	45	268	100	35	30.0	7	39.31	144.18
U3	18	45	268	100	35	30.0	7	39.82	144.01
U4	18	45	268	100	35	30.0	7	39.76	144.28
Compound mechanisms									
C11 = 0.8 * A2 + 0.2 * U1									
C12 = 0.8 * A2 + 0.2 * U2									
C13 = 0.8 * A3 + 0.2 * U3									
C14 = 0.8 * A3 + 0.2 * U4									

been extensively validated through comparisons with laboratory and field data, per standard international protocols; full details can be found in Synolakis (2003). We use a set of nested grids, the finest one sampling the Kona coast at a 1 arcsec interval (∼30 m) and the Honolulu shoreline at 2/3 arcsec (∼20 m). We compute time-series for 10 hr after origin time, or approximately 2.5 hr after arrival time in Hawaii. A significant difficulty in interpreting the 1933 run-up values involves the considerable development of the shorelines in the past 80 yr, in particular for Honolulu where the reef runway at Honolulu International Airport was built from landfill in the 1970s. In addition, we were unable to confirm the exact location of the Honolulu maregraph in 1933, and the assumption that it was installed at its present location (21.307°N, 157.867°W, next to the Aloha Tower passenger ship terminal) can only be tentative. Additionally, the exact locations for the run-up values reported on the Big Island of Hawaii are unknown, and these values must therefore be similarly qualified.

We use here a series of earthquake source models, listed in Table 4. For each of them, we compute a static vertical displacement of the sea floor, using Mansinha & Smylie's (1971) algorithm, and use it as an initial condition for the vertical displacement η of the ocean surface in the epicentral area.

We first consider single-fault models ('A') featuring the focal mechanism geometry derived on Fig. 7, with the westward-dipping plane as the fault plane ($\phi = 200°$, $\delta = 61°$ and $\lambda = 271°$). Model A1 has a fault length $L = 170$ km, as suggested by the extent of the subset of genuine aftershocks located oceanwards of the trench, and a slip of 18.5 m. These dimensions, which depart from classical seismic laws (e.g. Kanamori & Anderson 1975; Geller 1976), illustrate the 'snappy' character of the event, documented in Section 5. Model A2 uses an even larger slip (30 m) on a more compact fault. Models A3 and A4 displace the centroid of rupture 50 km along the strike of fault, NNE and SSW, respectively.

The choice of source models (A2, A3 and A4) featuring increased slip over a reduced fault zone deserves some comment. We concede that the fault length in such models (100 km) is significantly shorter than suggested (170 km) by the distribution of the so-called 'genuine' aftershocks taking place to the east of the trench, and generally interpreted as expressing the extent of coseismic faulting. We recall, however, the now classical case of the 2011 Tohoku earthquake, whose source involved a small patch of extremely large fault slip (∼60 m), concentrated on an asperity much smaller than the area of coseismic faulting, and which contributed the main tsunami genesis (Fujii *et al.* 2011; Lay *et al.* 2011). In a qualitatively similar fashion, in the case of the Aleutian earthquake of 1957 March 9, a discrepancy exists between the tsunamigenic source zone (extending 850 km, but concentrated mostly over 500 km) and the full extent of aftershocks (1200 km) (Johnson & Satake 1993; Johnson *et al.* 1994). In this context, source models with concentrated slip, such as A2, A3 and A4, are not necessarily incompatible with the distribution of the so-called 'genuine' aftershocks.

In addition, and following Uchida *et al.* (2016), we consider composite models ('C') defined as a combination of a primary, 'A'-type, source and an auxiliary one ('U'), featuring an oceanward-dipping mechanism ($\phi = 18°$, $\delta = 45°$ and $\lambda = 268°$), displaced to the west of the primary source. The strain release and fault aspect ratio of an auxiliary 'U' source are the same as for primary model A2, but the ratio of moment release between the two is left variable, while the total moment is kept at 7×10^{28} dyn cm. In this fashion, and given that the primary and auxiliary mechanisms share their neutral axis (see Appendix B), the composite source satisfies the mantle wave spectral data reported in Section 4. Auxiliary source U1 is displaced 50 km from A1 towards the coast of Japan, while source U2 is displaced only 25 km. Finally, U3 is moved NNE from U1 (and U4 from U2) by the same amount A3 is moved from A2.

We present here a number of representative models from a large set of 'A' and 'C' models. Figs 13–16 are organized as follows: Frames (a) show the static displacement in the source area, as obtained using Mansinha & Smylie's (1971) algorithm. Frames (b) and (c) map the maximum amplitude at sea, η_{max}, and run-up along the Kailua-Kona–Keauhou and Captain-Cook–Napoopoo sections of the Western coastline of the Big Island of Hawaii. Frames (d) similarly map the simulation of the tsunami along the Southern shore of Oahu, from Ewa Beach to Waikiki (using present-day bathymetry). Finally, frames (e) feature time-series simulated at the present location of the Honolulu maregraph (shown as a red triangle on frames (d)). They are designed to be compared with the maregram reproduced on Fig. 12.

Results for the simplest primary source, Model A1, are shown on Fig. 13. At Honolulu, while the general amplitude of the maregram (15 cm zero-to-peak) is adequately reproduced, the arrival of the tsunami remains emergent. In addition, run-up values in Kailua

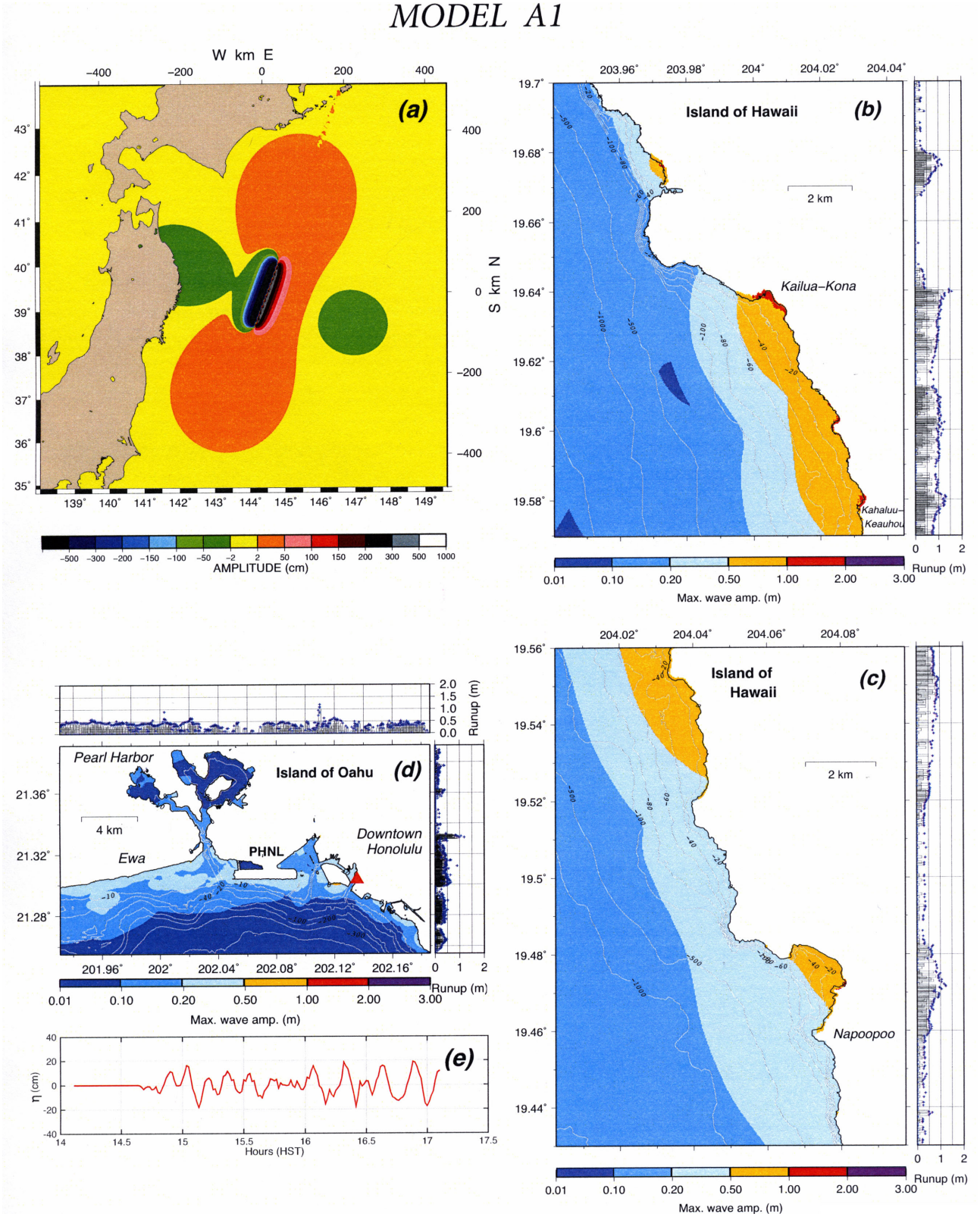

Figure 13. Tsunami simulation for Model A1 (see Table 4). (a) Map of static displacement in epicentral region, as computed using Mansinha & Smylie's (1971) algorithm, and used as initial condition in the simulation. (b) Maximum wave amplitude η_{max} simulated in the Kailua-Kona–Keauhou district of the Big Island, Note the weak inundation and run-up barely reaching 1 m. (c) Same as (b) for the Captain-Cook–Napoopoo district, approximately 7 km farther south. (d) Same as (b) for Downtown Honolulu. Note the use of present-day bathymetry, for example, the presence of the reef runway at Honolulu airport (PHNL). (e) Simulation of the Honolulu tide gauge record shown on Fig. 12, assuming its present location (red triangle on (d)). On frames (b)–(d), the horizontal bars at right (and on top in (d)) are simulated flow depths at individual locations along the coast, and the small blue dots the corresponding run-up values.

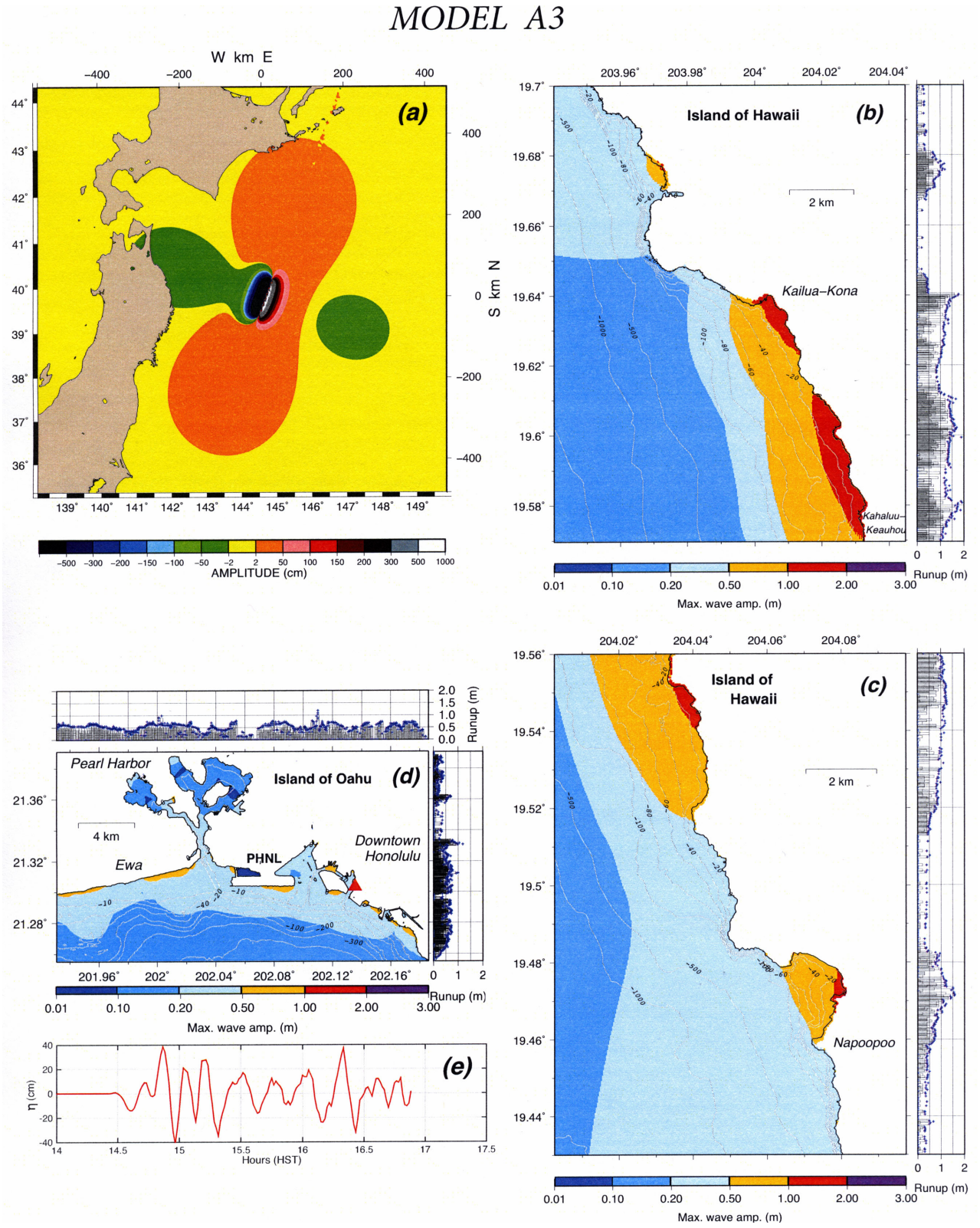

Figure 14. Same as Fig. 13 for Model A3, featuring a more compact source with larger slip, displaced 50 km to the NNE.

and Napoopoo barely reach 1 m and are thus clearly underestimating the observed data. This situation can be redressed by using a more concentrated source (A2), featuring a higher slip on a smaller fault, and thus a source blue-shifted towards higher frequencies and wavenumbers, delivering greater amplitude due to the non-linearity of the run-up process at the coast, even though all models share a constant seismic moment and thus should give rise to comparable far-field amplitudes on the high seas.

We also found that, under Model A3, displaced NNE 50 km along the fault strike, run-ups on the Big Island are further enhanced,

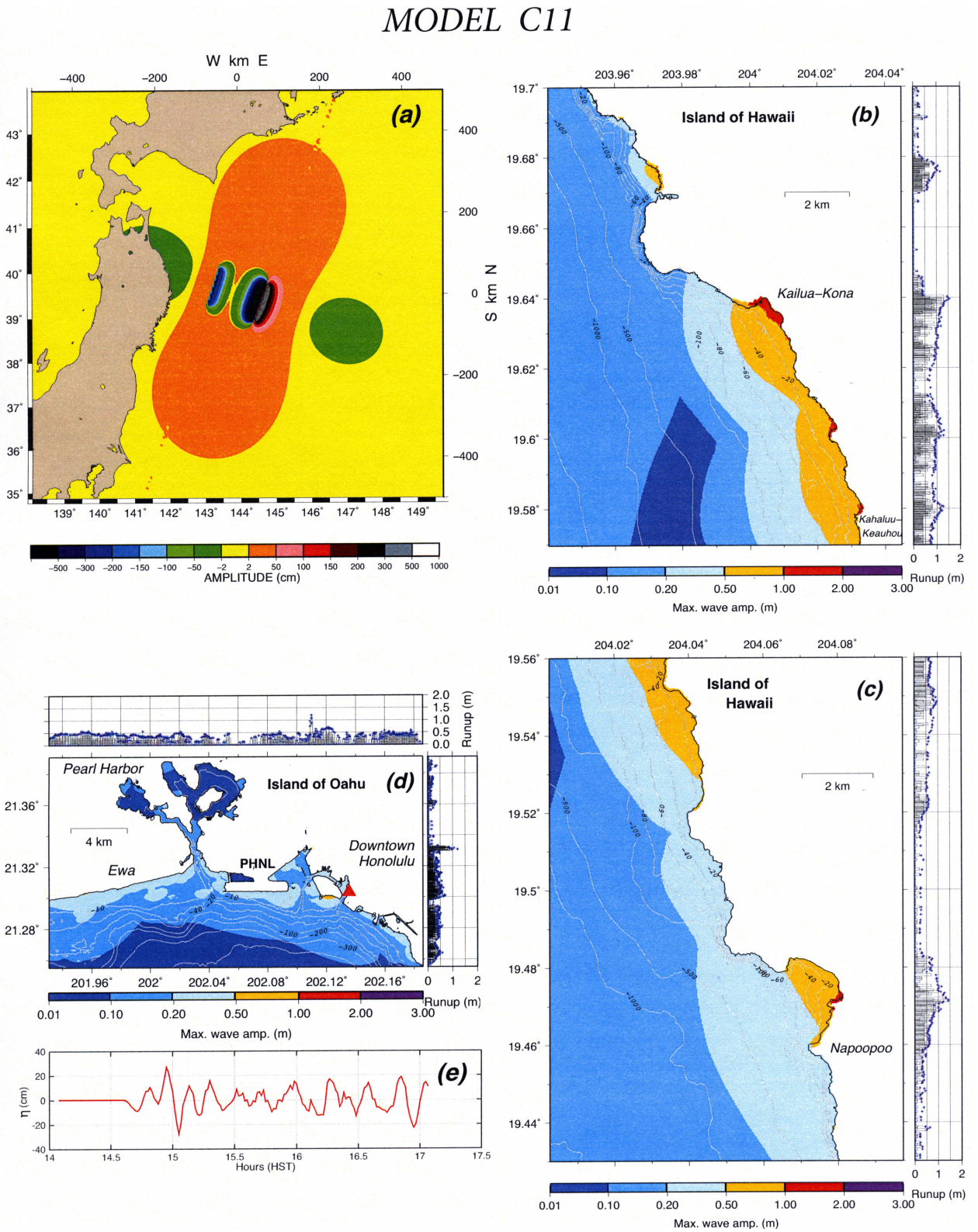

Figure 15. Same as Fig. 13 for Model C11. This compound source combines sources A2 (weighted 80 per cent) and U1 (weighted 20 per cent), the latter being an Uchida-type rupture offset 50 km to the WNW.

reaching 2 m in Kailua-Kona and Keauhou and 1.6 m at Napoopoo (Fig. 14). We have verified that moving the source slightly in the NNE direction results a small increase in average depth over the source area, which will result in larger amplitudes over a given ocean basin in the far field, as predicted under Green's (1837) law. While the values simulated under Model A3 still fall below the reported run-ups, they provide acceptable fits, given the uncertainty of their precise locations, and the possible change in local bathymetry and

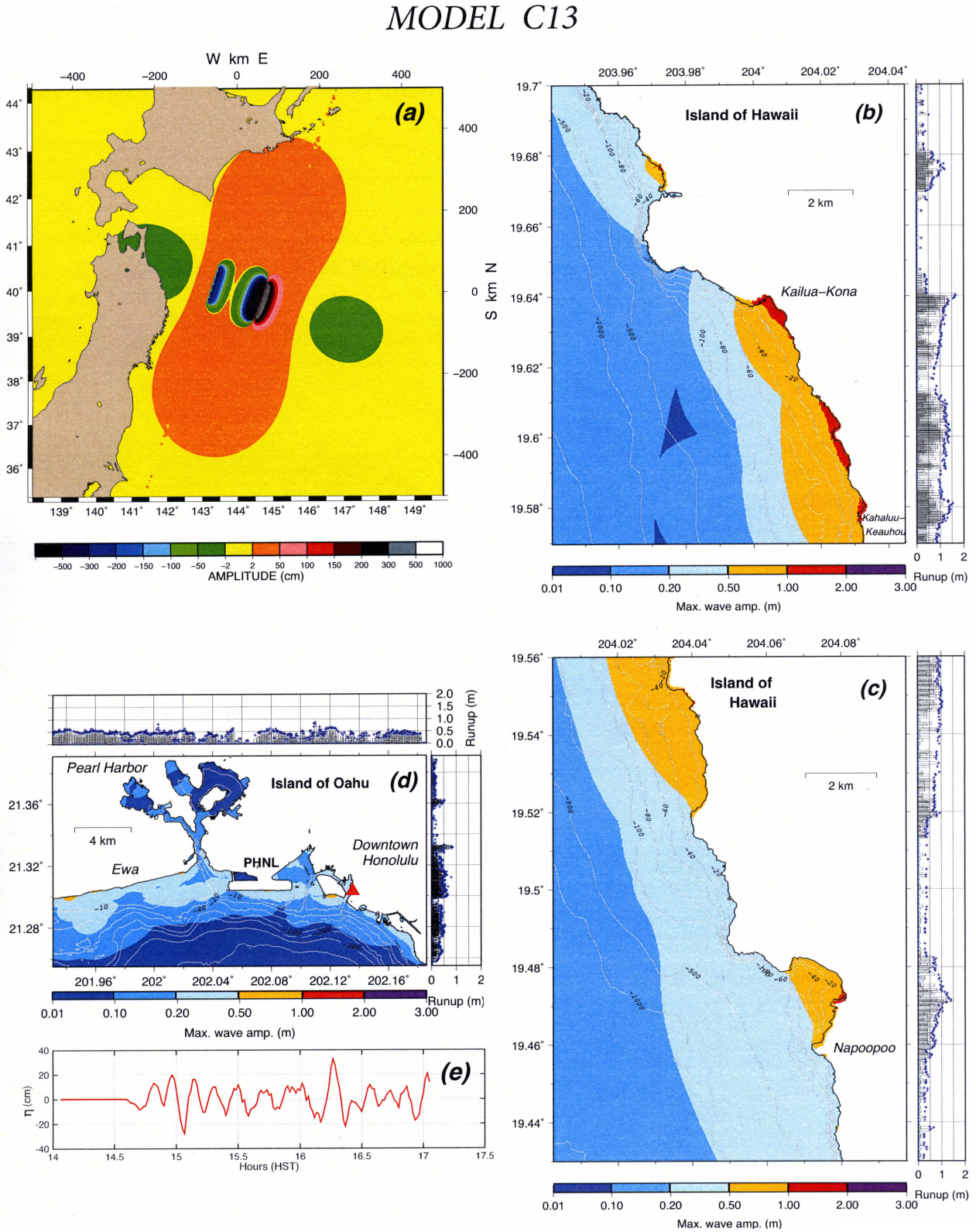

Figure 16. Same as Fig. 13 for Model C13. This source is just displaced 50 km to the NNE, with respect to C11.

topography in harbours which may have undergone development during the past 80 yr. In Honolulu, Model A3 yields a sharper, more impulsive first arrival of the wave (with the appropriate negative polarity), but a zero-to-peak amplitude of ∼40 cm, roughly twice as large as recorded.

The next model shown, on Fig. 15, is C11, a combination of 80 per cent of A2 (enhanced slip) and 20 per cent of the auxiliary model U1, thus keeping the total moment release of 7×10^{28} dyn cm. This results in weaker run-up amplitudes on the Big Island of Hawaii, most probably because of an increase in wavelengths,

due to a scattering of the initial displacement over a greater range of distances to the receiving shore. The use of U2, featuring a smaller spatial offset of Uchida *et al.*'s (2016) source relative to the primary one, actually reduces all measures of the tsunami amplitude (η_{max}, run-up), while source C13, that is, equivalent to C11 shifted NNE by 50 km, reduces run-up only marginally at Kailua-Kona and Napoopoo (Fig. 16). Finally, Model C13 gives an acceptable simulation of the Honolulu maregraph (including initial down-draw) and maximum amplitude.

7 CONCLUSIONS

A comprehensive study of seismological aspects of the Showa Sanriku earthquake of 1933 March 2 confirms its nature as the largest normal-faulting event ever recorded (with a seismic moment $M_0 = (7 \pm 1) \times 10^{28}$ dyn cm), occurring inside the incoming Pacific plate, in the outer slope of the trench. On the basis of its high energy-to-moment parameter, $\Theta = -4.24$, we characterize it as a fast, 'snappy' source, which also explains a wide variety of properties, including the distribution of isoseismals, the excessive magnitudes proposed by early investigators, and the most probable recording of a *T* wave at PAS. Such properties are similar to those observed in other cases of outer slope normal-faulting events, but the size of the 1933 earthquake remains exceptional.

Most importantly, our tsunami simulations, in particular those using the composite model proposed by Uchida *et al.* (2016), justify the order of magnitude of the run-up amplitudes reported on the Big Island of Hawaii and that of the Honolulu maregram. These results emphasize that sufficiently large normal-faulting events can contribute to tsunami hazard in the far field, and should therefore be taken into account when assessing such risks. While their apparent rarity (Kirby *et al.*, in preparation) acts in principle to minimize this risk, we presently ignore the precise tectonic conditions under which they can take place, and *a fortiori* any legitimate estimate of their recurrence times.

In the near field, the 1933 earthquake unleashed a tsunami which ran up to exceptional amplitudes, locally comparable to those of the great tsunamis of 1896 and 2011 along the Sanriku coast. This is in line with large run-ups observed during other normal-faulting events, such as the 1977 Sumbawa tsunami (Anonymous 1977). Incidentally, and as discussed in detail by Synolakis & Kânoğlu (2015), it remains unexplainable that the well-documented 1933 run-up values reaching 29 m at Yamada were ignored during the 2010 reassessment of the safety of the Fukushima Nuclear Power Plant with respect to tsunami risk, carried out only a few months before the 2011 disaster, and that an allegedly scientific examination of a 'worst case scenario' for a tsunami attack at the site concluded with a figure of 5.7 m, in rough numbers *five times* smaller than documented less than 80 yr earlier and only 200 km to the north.

In this context, we wish to guard against probabilistic estimates of tsunami risk at subduction zones most often based on the examination of convergence rates and thus tacitly but inescapably excluding the contribution of intraplate earthquakes, including large normal-faulting events, for which no reliable estimate of recurrence times is available. Yet, these events are a significant ingredient to the quantitative budget of the Earth's seismicity, as witnessed not only by the Showa Sanriku earthquake, but also by such events as the 1977 Sumbawa, 1975 East Luzon and probably 1915 Central Kuril earthquakes, the first two representing the largest tsunami contributors at their respective plate boundaries. Over and beyond the case of the Showa Sanriku earthquake, these remarks mandate the deterministic inclusion of normal-faulting intraplate events in any assessment of tsunami risk at subduction zones worldwide.

ACKNOWLEDGEMENTS

We are grateful to Hiroo Kanamori for sending us a preliminary write up of his solution for the moment of the 1933 earthquake, and to Naoki Uchida for collaboration and a data set of Uchida *et al.* (2016) relocations. We thank Roger Buck for discussions on stress release in the upper plate, Norihito Umino for access to T. Matuzawa's collection of original seismograms and to the Omori records from the Mizusawa archives, and Takeo Ishibe for a data set of intensity values during the 2011 Tohoku earthquake. EAO was partially supported by the National Science Foundation, under subcontract from the University of Pittsburgh's Hazards SEES Grant number OCE-1331463; NK enjoyed support from the National Science Foundation under Grant CMI-1538624 to the University of Southern California. The paper was improved through the comments of two anonymous reviewers. Some figures were plotted using the GMT software (Wessel & Smith 1991).

REFERENCES

Abe, K., 1972. Lithospheric normal faulting beneath the Aleutian trench, *Phys. Earth planet. Inter.,* **5,** 190–198.

Ammon, C.J., Kanamori, H. & Lay, T., 2008. A great earthquake doublet and seismic stress transfer cycle in the central Kuril Islands, *Nature,* **451,** 561–565.

Anonymous, 1934. Papers and reports on the tsunami of 1933 on the Sanriku coast, Japan, *Bull. Earthq. Res. Inst. Tokyo Univ.,* **8**(1), 7–8 and Pl. X.

Anonymous, 1977. Indonesian tsunami of August 19, 1977, *Tsunami Newsl.,* **10**(3), 1–3.

Atkinson, G.M. & Wald, D.J., 2007. 'Did you feel it?' Intensity data: a surprisingly good measure of earthquake ground motion, *Seismol. Res. Lett.,* **78,** 362–368.

Benioff, V.H., 1932. A new vertical seismograph, *Bull. seism. Soc. Am.,* **22,** 155–169.

Benioff, V.H., 1935. A linear strain seismograph, *Bull. seism. Soc. Am.,* **25,** 283–309.

Ben-Menahem, A., 1977. Renormalization of the magnitude scale, *Phys. Earth planet. Inter.,* **15,** 315–340.

Boatwright, J. & Choy, G.L., 1986. Teleseismic estimates of the energy radiated by shallow earthquakes, *J. geophys. Res.,* **91,** 2095–2112.

Borrero, J.C., Ortíz, M., Titov, V.V. & Synolakis, C.E., 1997. Field survey of Mexican tsunami produces new data, unusual photos, *EOS, Trans. Am. geophys. Un.,* **78,** 85 and 87–88.

Brune, J.N. & Engen, G.R., 1969. Excitation of mantle Love waves and definition of mantle wave magnitude, *Bull. seism. Soc. Am.,* **59,** 923–933.

Buck, W.R., Lavier, L. & Petersen, K.D., 2015. Extensional failure of 'pre-stressed' lithosphere above a subduction zone may have contributed to the size of the Tohoku-Oki earthquake and tsunami, *EOS, Trans. Am. geophys. Un.,* **96** (53), T12C-01 [abstract].

Chapple, W.M. & Forsyth, D.W., 1979. Earthquakes and bending of plates at trenches, *J. geophys. Res.,* **84,** 6729–6749.

Chen, T. & Forsyth, D.W., 1978. A detailed study of two earthquakes seaward of the Tonga Trench: implications for mechanical behavior of the oceanic lithosphere, *J. geophys. Res.,* **83,** 4995–5003.

Choy, G.L. & Kirby, S.H., 2004. Apparent stress, fault maturity and seismic hazard for normal-fault earthquakes at subduction zones, *Geophys. J. Int.,* **159,** 991–1012.

Choy, G.L., Boatwright, J. & Kirby, S.H., 2001. The radiated seismic energy and apparent stress of interplate and intraslab earthquakes at subduction zone environments: Implications for seismic hazard estimation. USGS Open File Rep., 01–0005, 18 pp.

Dziewoński, A.M., Ekström, G., Franzen, J.E. & Woodhouse, J.H., 1987. Global seismicity of 1977; Centroid moment tensor solutions for 471 earthquakes, *Phys. Earth planet. Inter.,* **45,** 11–36.

Engdahl, E.R. & Villaseñor, A., 2002. Global seismicity: 1900–1999, in *International Earthquake and Engineering Seismology Part A,* pp. 665–690, Elsevier, New York.

Fujii, Y., Satake, K., Sakai, S., Shinohara, M. & Kanazawa, T., 2011. Tsunami source of the 2011 off the Pacific coast of Tohoku earthquake, *Earth Planet Space,* **63,** 815–820.

Fukuchi, T. & Mitsuhashi, K., 1983. Tsunami countermeasures in fishing villages along the Sanriku coast, Japan, in *Tsunamis - Their Science and Engineering,* pp. 389–396, eds Iida, K. & Iwasaki, T., TERRAPUB, Tokyo.

Gamage, S.S.N., Umino, N., Hasegawa, A. & Kirby, S.H., 2009. Offshore double-planed shallow seismic zone in the NE Japan forearc region revealed by *sP* depth phases recorded by regional networks, *Geophys. J. Int.,* **178,** 195–214.

Geller, R.J., 1976. Scaling relations for earthquake source parameters and magnitudes, *Bull. seism. Soc. Am.,* **66,** 1501–1523.

Glover, D.P. & Meyers, H., 1987. Historical seismogram filming project: current status, in *Historical Seismograms and Earthquakes of the World,* pp. 373–379, eds Lee, W.H.K., Meyers, H. & Shimazaki, K., Academic Press, San Diego.

Godunov, S.K., 1959. Finite difference methods for numerical computations of discontinuous solutions of the equations of fluid dynamics, *Matemat. Sb.,* **47,** 271–295.

Goodstein, J.R. & Roberts, P., 1987. Filming seismograms and related materials at the California Institute of Technology, in *Historical Seismograms and Earthquakes of the World,* pp. 380–389, eds Lee, W.H.K., Meyers, H. & Shimazaki, K., Academic Press, San Diego.

Goodstein, J.R., Kanamori, H.H. & Lee, W.H.K., 1980. Seismology microfiche publications from the Caltech archives, *Bull. seism. Soc. Am.,* **70,** 657–658.

Govers, R. & Wortel, M.J.R., 2005. Lithosphere tearing at STEP faults: response to edges of subduction zones, *Earth planet. Sci. Lett.,* **236,** 505–523.

Green, G., 1837. On the motion of waves in a canal of variable depth, *Camb. Phil. Trans.,* **6,** 457–462.

Gutenberg, B. & Richter, C.F., 1936. On seismic waves (Third paper), *Gerlands Beitr. Geophys.,* **47,** 73–131.

Gutenberg, B. & Richter, C.F., 1941. *Seismicity of the Earth,* 1st edn, Geol. Soc. Amer., Sp. Paper **34,** 125 pp.

Gutenberg, B. & Richter, C.F., 1954. *Seismicity of the Earth and Associated Phenomena,* 2nd edn, Princeton Univ. Press, 310 pp.

Honda, H. & Takehana, M., 1933. Results from the survey of the severe earthquake offshore Sanriku, *Kensin Zihô,* **7,** 197–213 [in Japanese].

Iida, K., Cox, D.C. & Pararas-Carayannis, G., 1967. Preliminary catalog of tsunamis occurring in the Pacific Ocean. Data Rep. 5, HIG-67-10, Hawaii Inst. Geophys., Univ. Hawaii, Honolulu.

Ishimoto, M., 1933. Preliminary notes on the tunami of March 2, 1933 (GMT), and an outline of the investigations now made concerning it at the Earthquake Research Institute, *Jap. J. Astron. Geophys.,* **11,** 1–10.

Jaggar, T., 1930. *The Volcano Letter,* Vol. 274, pp. 1–4.

Jaggar, T., 1933. *The Volcano Letter,* Vol. 397, pp. 1–2.

Johnson, J.M. & Satake, K., 1993. Source parameters of the 1957 Aleutian earthquake from tsunami waveforms, *Geophys. Res. Lett.,* **20,** 1487–1490.

Johnson, J.M., Tanioka, Y., Ruff, L.J., Satake, K., Kanamori, H. & Sykes, L.R., 1994. The 1957 great Aleutian earthquake, *Pure appl. Geophys.,* **142,** 3–28.

Kagan, Y.Y., 1991. 3-D rotation of double-couple earthquake sources, *Geophys. J. Int.,* **106,** 709–716.

Kanamori, H., 1971. Seismological evidence for a lithospheric normal faulting—The Sanriku earthquake of 1933, *Phys. Earth planet. Inter.,* **4,** 289–300.

Kanamori, H., 1972. Mechanism of tsunami earthquakes, *Phys. Earth planet. Inter.,* **6,** 346–359.

Kanamori, H. & Anderson, D.L., 1975. Theoretical basis of some empirical relations in seismology, *Bull. seism. Soc. Am.,* **65,** 1073–1095.

Kanamori, H. & Cipar, J.J., 1974. Focal process of the great Chilean earthquake, May 22, 1960, *Phys. Earth planet. Inter.,* **9,** 128–136.

Kanamori, H., Rivera, L. & Lee, W.H.K., 2010. Historical seismograms for unraveling a mysterious earthquake: The 1907 Sumatra Earthquake, *Geophys. J. Int.,* **183,** 358–374.

Lay, T., Ammon, C.J., Kanamori, H., Rivera, L., Koper, K.D. & Hutko, A.R., 2010. The Samoa-Tonga great earthquake triggered doublet, *Nature,* **466,** 964–968.

Lay, T., Ammon, C.J., Kanamori, H., Xue, L. & Kim, M., 2011. Possible large near-trench slip during the 2011 $M_w = 9.0$ off the Pacific coast of Tohoku earthquake, *Earth Planet Space,* **63,** 687–692.

Li, X., Shao, G. & Ji, C., 2009. Rupture process of $M_w = 8.1$ Samoa earthquake constrained by joint inverting teleseismic body, surface waves and local strong motion, *EOS, Trans. Am. geophys.Un.,* **90**(53), U21D–03 [abstract].

Lin, J. & Stein, R.S., 2004. Stress triggering in thrust and subduction earthquakes and stress interaction between the southern San Andreas and nearby thrust and strike-slip faults, *J. geophys. Res.,* **109**(B2), B02303, doi:10.1029/2003JB002607.

Mansinha, L. & Smylie, D.E., 1971. The displacement fields of inclined faults, *Bull. seism. Soc. Am.,* **61,** 1433–1440.

Matuzawa, T., 1935. Seismometrische Untersuchungen des Erdebebens vom 2. März 1933. I. Bestimmung des Herdes, *Bull. Earthq. Res. Inst. Tokyo Univ.,* **13,** 171–193.

Matuzawa, T., 1942. Seismometrische Untersuchungen des Erdebebens vom 2. März 1933. IV. Raumverteilung der Wellenstrahlung aus dem Herd, *Bull. Earthq. Res. Inst. Tokyo Univ.,* **20,** 162–171.

Newman, A.V. & Okal, E.A., 1998. Teleseismic estimates of radiated seismic energy: the E/M_0 discriminant for tsunami earthquakes, *J. geophys. Res.,* **103,** 26 885–26 898.

Okal, E.A., 1992. Use of the mantle magnitude M_m for the reassessment of the seismic moment of historical earthquakes. I: shallow events, *Pure appl. Geophys.,* **139,** 17–57.

Okal, E.A., 2007. The generation of *T* waves by earthquakes, *Adv. Geophys.,* **49,** 1–65.

Okal, E.A., 2008. The excitation of tsunamis by earthquakes, in *The Sea: Ideas and Observations on Progress in the Study of the Seas,* Vol. 15, pp. 137–177, eds Bernard, E.N. & Robinson, A.R., Harvard Univ. Press, Cambridge.

Okal, E.A. & Hartnady, C.J., 2009. The South Sandwich Islands earthquake of 27 June 1929: seismological study and inference on tsunami risk for the South Atlantic, *S. Afr. J. Geol.,* **112,** 359–370.

Okal, E.A. & Kirby, S.H., 2002. Energy-to-moment ratios for damaging intraslab earthquakes: preliminary results on a few case studies, *USGS Open File Rep.,* 02–328, 127–131.

Okal, E.A. & Reymond, D., 2003. The mechanism of the great Banda Sea earthquake of 01 February 1938: applying the method of Preliminary Determination of Focal Mechanism to a historical event, *Earth planet. Sci. Lett.,* **216,** 1–15.

Okal, E.A., Alasset, P.-J., Hyvernaud, O. & Schindelé, F., 2003. The deficient *T* waves of tsunami earthquakes, *Geophys. J. Int.,* **152,** 416–432.

Okal, E.A., Hongsresawat, S. & Stein, S., 2012. Split mode evidence for no ultra-slow component to the source of the 2010 Maule, Chile earthquake, *Bull. seism. Soc. Am.,* **102,** 391–397.

Rees, B.A. & Okal, E.A., 1987. The depth of the deepest historical earthquakes, *Pure appl. Geophys.,* **125,** 699–715.

Reymond, D. & Okal, E.A., 2000. Preliminary determination of focal mechanisms from the inversion of spectral amplitudes of mantle waves, *Phys. Earth planet. Inter.,* **121,** 249–271.

Richter, C.F., 1935. An instrumental magnitude scale, *Bull. seism. Soc. Am.,* **25,** 1–32.

Richter, C.F., 1958. *Elementary Seismology,* W.H. Freeman and Co., 768 pp.

Romanowicz, B. & Suárez, G., 1983. An improved method to obtain the moment tensor depth of earthquakes from the amplitude spectrum of Rayleigh waves, *Bull. seism. Soc. Am.,* **73,** 1513–1526.

Solov'ev, S.L. & Go, Ch.N., 1984. Catalogue of tsunamis on the Western shore of the Pacific Ocean, *Can. Transl. Fish. Aquat. Sci.,* **5077,** 439 pp.

Stauder, W.J., 1968a. Mechanism of the Rat Island sequence of February 4, 1965, with relation to island arcs and sea-floor spreading, *J. geophys. Res.,* **73,** 3847–3858.
Stauder, W.J., 1968b. Tensional character of earthquake foci beneath the Aleutian Trench with relation to sea-floor spreading, *J. geophys. Res.,* **73,** 7693–7701.
Stein, R.S., 1999. The role of stress transfer in earthquake occurrence, *Nature,* **402,** 605–609.
Synolakis, C.E., 2003. Tsunami and seiche, in *Earthquake Engineering Handbook,* pp. 9_1–9_90, eds Chen, W.-F. & Scawthron, C., CRC Press, Boca Raton.
Synolakis, C.E. & Kânoğlu, U., 2015. The Fukushima accident was preventable, *Phil. Trans. R. Soc. Lond. A,* **373,** 20140379, 26 pp.
Tadepalli, S. & Synolakis, C.E., 1996. Model for the leading waves of tsunamis, *Phys. Rev. Lett.,* **77,** 2141–2145.
Titov, V.V. & Synolakis, C.E., 1998. Numerical modeling of tidal wave runup, *J. Wtrwy. Port Coast. Eng.,* **124,** 157–171.
Uchida, N., Kirby, S., Umino, N., Hino, R. & Kazakami, T., 2016. The great 1933 Sanriku-oki earthquake: reappraisal of the mainshock and its aftershocks and implications for its tsunami using regional tsunami and seismic data, *Geophys. J. Int.,* doi:10.1093/gji/ggw234.
Vaněk, J., Zátopek, A., Kárník, V., Kondorskaya, N.V., Riznichenko, Yu.V., Savarenskiĭ, E.F., Solov'ev, S.L. & Shebalin, N.V., 1962. Standardization of magnitude scales, *Izv. Akad. Nauk SSSR, Ser. Geofiz.,* **2,** 153–158.
Wessel, P. & Smith, W.H.F., 1991. Free software helps map and display data, *EOS, Trans. Am. geophys. Un.,* **72,** 441 and 445–446.
Wong, H.L. & Trifunac, M.D., 1979. A note on an instrumental comparison of the Modified Mercalli (MMI) and the Japanese Meteorological Agency (JMA) intensity scales, based on computed peak accelerations, *Earthq. Eng. Struct. Dyn.,* **7,** 75–83.
Wysession, M.E., Okal, E.A. & Miller, K.L., 1991. Intraplate seismicity of the Pacific Basin, 1913–1988, *Pure appl. Geophys.,* **135,** 261–359.

APPENDIX A: INSTRUMENT RESPONSE OF THE SHORT-PERIOD BENIOFF SEISMOMETERS IN 1933

In the early 1930s, Benioff (1932) was developing his short-period seismometers, of which a number had been deployed in Southern California by the time of the 1933 Sanriku earthquake; Matuzawa (1935; fig. 3b) published an excellent photographic excerpt of the RVR record, which clearly features a *P* waveform richer in high frequencies than recorded by the more classical torsion instruments. Such excellent records are available on microfilm from the U.S. Geological Survey (Goodstein & Roberts 1987) as part of the Historical Seismogram Filming Project (Glover & Meyers 1987), and can provide exceptional insight into the high-frequency characteristics of the source. However, there remains some uncertainty regarding the exact constants used on the Benioff short-period instruments at the time of the 1933 Sanriku earthquake, most crucially regarding overall magnification.

The constants of the short-period Benioff instrument (which were to be used later for the short-period WWSSN seismograph) were adopted definitively around 1934 with a pendulum period $T_p = 1$ s and a galvanometer period $T_g = 0.2$ (or 0.23) s. However, in the early stages of development, a pendulum period of 0.5 s was used (as documented for example in the caption to Matuzawa's (1935) reproduction of the records), and H. Benioff also experimented with various values of T_g, ranging from 0.2 s (as used in RVR) to 1.5 s (as used on the vertical seismometer in PAS); the difference in response at the two stations is obvious on fig. 3 of Matuzawa (1935). However, the PAS NS instrument was apparently operated with $T_g = 0.2$ s. As for the gains, Benioff (1932) states that the system could be operated in the 'Moll configuration' with a gain of 100 000 (this figure representing the maximum gain of the system), but that it became sensitive to human noise at such high gains; indeed, several years later, the PAS system had been standardized to a gain of 30 000 (with also the longer $T_p = 1$ s). Note in particular that Benioff's paper is timelined 1932 January 16, more than a year before the Sanriku earthquake, leaving ample time for probable further adjustments of its magnification during what were the final stages of the development of the instrument. In this respect, a ledger of handwritten notes from the Pasadena Seismological Laboratory archives indicates that on 1932 November 1, a short-period instrument (presumably the NS one) was being operated with $T_g = 0.2$ s and a magnification of 80 000 (Kanamori, personal communication, 2011). Ledger notes for late 1932 as well as a barely legible one, probably referring to 1933, repeat this value of the magnification, and we will therefore use it henceforth, but emphasize that it remains tentative. At any rate it represents a maximum magnification, reached around $T = 0.2$ s, while at $T = 1$ s, the gain has fallen by a factor of 11.7 to 6840.

We could not find any direct information on the gain of the vertical Benioff short-period instruments operated in 1933 at MWC and RVR. However, a comparison of the digitized traces of the *P*-wave groups at PAS (horizontal component), and MWC and RVR (vertical) suggests that the latter may have been operating with gains of 50 000 and 30 000, respectively.

APPENDIX B: COMBINING DOUBLE-COUPLES

We derive here three theorems related to the moment tensor resulting from summing double-couples which share certain elements.

Lemma. *Any symmetric* 2×2 *matrix* $\mathbf{M}$ *with zero-trace and negative determinant* Δ *can be written as* $\mathbf{M} = M_0[\hat{\delta}\hat{\nu}^{\mathrm{T}} + \hat{\nu}\hat{\delta}^{\mathrm{T}}]$ *where* $\hat{\delta}$ *and* $\hat{\nu}$ *are two unit vectors perpendicular to each other* ($M_0 > 0$). *This represents the projection of a double-couple on the plane perpendicular to its null axis.*

Proof: Define $M_0 = \sqrt{-\Delta}$ and $\mathbf{N} = \mathbf{M}/M_0$. Then $\mathbf{N}$ is symmetric, has zero trace and a determinant equal to -1. It can be written as

$$\mathbf{N} = \begin{pmatrix} -a & b \\ b & a \end{pmatrix} \tag{B1}$$

with $a^2 + b^2 = 1$. Set $a = \sin 2\phi$; $b = \cos 2\phi$. Define $\hat{\delta} = \begin{pmatrix} \cos\phi \\ \sin\phi \end{pmatrix}$; $\hat{\nu} = \begin{pmatrix} -\sin\phi \\ \cos\phi \end{pmatrix}$

Then

$$\hat{\delta}\hat{\nu}^{\mathrm{T}} + \hat{\nu}\hat{\delta}^{\mathrm{T}} = \begin{pmatrix} -\sin\phi\cos\phi & \cos^2\phi \\ \cos^2\phi & \sin\phi\cos\phi \end{pmatrix} + \begin{pmatrix} -\sin\phi\cos\phi & -\sin^2\phi \\ -\sin^2\phi & \sin\phi\cos\phi \end{pmatrix} = \begin{pmatrix} -\sin 2\phi & \cos 2\phi \\ \cos 2\phi & \sin 2\phi \end{pmatrix} = \mathbf{N} \tag{B2}$$

Q.E.D.

Theorem 1. *Any superposition of two double-couples which share a null axis* $\hat{\mathbf{b}}$ *makes up a pure double-couple.*

Proof: In the plane perpendicular to $\hat{\mathbf{b}}$, define unit vectors $\hat{\mathbf{d}}_1$ and $\hat{\mathbf{n}}_1$ along slip and normal to fault plane of the first double-couple, $\hat{\mathbf{d}}_2$ and $\hat{\mathbf{n}}_2$ for the second double-couple. Let x be the moment of the second double-couple relative to the first one. Let θ be the angle between $\hat{\mathbf{d}}_1$ and $\hat{\mathbf{d}}_2$.

In the frame $(\hat{\mathbf{d}}_1, \hat{\mathbf{n}}_1)$, the projection of the first double-couple is

$$\mathbf{M}_1 = \begin{pmatrix} 1 \\ 0 \end{pmatrix} (0 \;\; 1) + \begin{pmatrix} 0 \\ 1 \end{pmatrix} (1 \;\; 0) = \begin{pmatrix} 0 & 1 \\ 1 & 0 \end{pmatrix} \tag{B3}$$

The projection of the second double-couple is

$$\mathbf{M}_2 = x \left[\begin{pmatrix} \cos\theta \\ \sin\theta \end{pmatrix} (-\sin\theta \;\; \cos\theta) + \begin{pmatrix} -\sin\theta \\ \cos\theta \end{pmatrix} (\cos\theta \;\; \sin\theta) \right]$$

$$= x \begin{bmatrix} -\sin 2\theta & \cos 2\theta \\ \cos 2\theta & \sin 2\theta \end{bmatrix} \tag{B4}$$

so that the combination of the two double-couples, projected perpendicular to $\hat{\mathbf{b}}$, is

$$\mathbf{M_c} = \mathbf{M_1} + \mathbf{M_2} = \begin{pmatrix} -x\sin 2\theta & 1 + x\cos 2\theta \\ 1 + x\cos 2\theta & x\sin 2\theta \end{pmatrix} \tag{B5}$$

The matrix $\mathbf{M}_c$ is obviously symmetric, has zero trace, and its determinant

$$\Delta = -x^2 \sin^2 2\theta - (1 + x\cos 2\theta)^2 \tag{B6}$$

is negative. Applying the lemma, $\mathbf{M}_c$ represents the projection on the plane of a double-couple of null axis $\hat{\mathbf{b}}$. **Q.E.D.**

Theorem 2. *Any combination of double-couples sharing their vectors* $\hat{\mathbf{n}}$ *(i.e. sharing a fault plane) makes up a pure double-couple.*

Proof: Consider two double-couples

$$\mathbf{M_1} = \hat{\mathbf{n}}\hat{\mathbf{d}}_1^{\mathrm{T}} + \hat{\mathbf{d}}_1\hat{\mathbf{n}}^{\mathrm{T}};\; \mathbf{M_2} = x \cdot \left[\hat{\mathbf{n}}\hat{\mathbf{d}}_2^{\mathrm{T}} + \hat{\mathbf{d}}_2\hat{\mathbf{n}}^{\mathrm{T}}\right]. \tag{B7}$$

Their sum can be written

$$\mathbf{M}_c = \hat{\mathbf{n}}\left(\hat{\mathbf{d}}_1^{\mathrm{T}} + x\hat{\mathbf{d}}_2^{\mathrm{T}}\right) + \left(\hat{\mathbf{d}}_1 + x\hat{\mathbf{d}}_2\right)\hat{\mathbf{n}}^{\mathrm{T}} = M_0 \cdot \left(\hat{\mathbf{n}}\hat{\mathbf{d}}_{\mathbf{c}}^{\mathrm{T}} + \hat{\mathbf{d}}_{\mathbf{c}}\hat{\mathbf{n}}^{\mathrm{T}}\right) \tag{B8}$$

if we define M_0 and $\hat{\mathbf{d}}_c$ so that

$$M_0\hat{\mathbf{d}}_{\mathbf{c}} = \hat{\mathbf{d}}_1 + x\hat{\mathbf{d}}_2 \tag{B9}$$

with $\hat{\mathbf{d}}_c$ a unit vector, and $M_0 > 0$. **Q.E.D.**

Theorem 3. *Any combination of double-couples sharing their vectors* $\hat{\mathbf{d}}$ *(i.e. sharing slip vectors) makes up a pure double-couple.*

Proof: For both double-couples, consider the conjugate solutions, for which the vectors $\hat{\mathbf{n}}$ and $\hat{\mathbf{d}}$ are permuted. These new solutions now share their fault planes. Apply Theorem 2; they combine into a double-couple. **Q.E.D.**

It is interesting to note that Theorems 2 and 3 are valid for double-couples sharing either their slip vectors or [normals to] the fault planes, but would not hold for events sharing either **P** or **T** axes.